



THE UNIVERSITY *of* EDINBURGH

Edinburgh Research Explorer

## 4D porosity evolution during pressure-solution of NaCl in the presence of phyllosilicates

### Citation for published version:

Macente, A, Fousseis, F, Butler, I, Tudisco, E, Hall, SA & Andò, E 2018, '4D porosity evolution during pressure-solution of NaCl in the presence of phyllosilicates', *Earth and Planetary Science Letters*, vol. 502, pp. 115-125. <https://doi.org/10.1016/j.epsl.2018.08.032>

### Digital Object Identifier (DOI):

[10.1016/j.epsl.2018.08.032](https://doi.org/10.1016/j.epsl.2018.08.032)

### Link:

[Link to publication record in Edinburgh Research Explorer](#)

### Document Version:

Peer reviewed version

### Published In:

Earth and Planetary Science Letters

### General rights

Copyright for the publications made accessible via the Edinburgh Research Explorer is retained by the author(s) and / or other copyright owners and it is a condition of accessing these publications that users recognise and abide by the legal requirements associated with these rights.

### Take down policy

The University of Edinburgh has made every reasonable effort to ensure that Edinburgh Research Explorer content complies with UK legislation. If you believe that the public display of this file breaches copyright please contact [openaccess@ed.ac.uk](mailto:openaccess@ed.ac.uk) providing details, and we will remove access to the work immediately and investigate your claim.



Manuscript Number: EPSL-D-18-00325R2

Title: 4D porosity evolution during pressure-solution of NaCl in the presence of phyllosilicates

Article Type: Letters

Keywords: pressure-solution creep; phyllosilicates; X-ray microtomography; Digital Volume Correlation; geochemical self-organization

Corresponding Author: Dr. Alice Macente, Ph.D

Corresponding Author's Institution: Stanford University

First Author: Alice Macente, Ph.D

Order of Authors: Alice Macente, Ph.D; Florian Fuisseis; Ian B Butler; Erika Tudisco; Stephen A Hall; Edward Andò

Abstract: Pressure-solution creep is one of the most common crustal deformation mechanisms, inducing changes in the porosity and permeability of rocks. For a variety of rock types undergoing pressure solution, it has been shown that the presence of phyllosilicates may significantly enhance the rate of the pressure-solution process. In this experimental investigation, we present 4-dimensional (three dimensions + time) X-ray microtomographic data that contrast deformation by pressure-solution of a pure NaCl aggregate with that of a mixture of NaCl and biotite. The results show that for mixed samples (NaCl+biotite), phyllosilicates induce a marked reduction in porosity and pore connectivity and contribute to an increase in the local strain rates by an order of magnitude over pure NaCl samples. At the same time, phyllosilicates do not induce strain localization in the sample. We discuss various possible explanations for these observations including a possible positive feedback between the porosity distribution and pressure solution. Our study yields novel insights into the local effects of phyllosilicates during pressure-solution creep and provides full 4-dimensional imaging and characterization of the coupled evolution of porosity and pore connectivity over previously unprecedented experimental time scales.

## Rebuttal/list of changes

The discussion can be stronger in determining the potential reasons for the decreased porosity in the biotite zone, and what the relative importance is of these different reasons. The dismissal and acceptance of hypotheses can be better correlated to the images obtained. I do not see how the force chains come in, or where they are shown on the image. Nor am I certain I can see the locations of increased dissolution and preferred location precipitation (last hypothesis), though I do think this hypothesis sounds the most plausible. Perhaps also it can be a combination of the different hypothesis mentioned, where some play a role during fast early compaction, and others during the slower aftermath. Additionally, the comparison with previous literature could also be stronger, i.e. Renard et al indicate a mechanical role of clay particles, which is not mentioned by the authors here. Spiers et al compacted similar size NaCl aggregates and obtained different strain rates at lower stresses. What are the differences between their and these results? In the line-by-line comments on the discussion there are some more details on which lines can use some clarification.

We thank the reviewer for these additional comments and her opinion on our manuscript. In the line-by-line comments, we respond to the reviewer's comments. Combined, they form our response to the points raised above.

### *Line-by-line comments*

1. Highlight 1 & 2 are very similar

We removed the second highlight to improve clarity.

2. Highlight 1: isn't it local porosity, not bulk? Porosity outside biotite zones is less affected. The term bulk porosity implies the complete sample to me.

We agree with the reviewer's comment and changed the text accordingly.

3. Line 20: To avoid confusion (since you didn't test all phyllosilicates) I would suggest rephrasing to 'the results show that for mixed samples (NaCl+biotite), the phyllosilicates induce'

We revised the text according to the reviewer's suggestion.

4. Line 44: somewhat arbitrary selection of references; already from your own reference list you could create a more diverse list of geological materials (from your list you could include: Bos and Spiers - phyllosilicates, Pluymakers and Spiers - anhydrite). Moreover, since there definitely exist other geomaterials than listed here, I'd suggest preceding these references with e.g.

The reference list was modified to include the suggestion of the reviewer.

5. Line 46: change to 'these alterations, may, in turn' - a change in transport properties is not a given - that would depend on the amount of alteration and potentially also direction of transport

We agree and we change the text accordingly.

6. Line 79-80: why not both? i.e. leave the NaCl as geomaterials, since they are geomaterials in salt deposits, and if you want you can state here that they are often used as analogues for

other rock combinations that deform slower, with the appropriate references? This would make more sense than denying NaCl is a geomaterial

We have been careful with our choice of words. We agree that NaCl is a geomaterial in its own right, however, we do note that natural evaporites undergoing deformation do not occur in the form used in these experiments, i.e. highly porous granular NaCl aggregates. Nevertheless, in that form NaCl does provide a useful experimental analogue for other granular geomaterials.

7. Line 102: 'dimensions of the initial salt stack' is this from the reference scan, i.e. after pre-compaction? Unclear

Yes, the dimension of the initial salt scan refers to the reference scan. We modified the text to improve clarity.

8. Figure S2 caption: is this the NaCl+bio sample presented in the main paper or the one presented in the supplementary material?

The caption refers to the NaCl-biotite sample presented in the main paper. The second NaCl-biotite sample presented in the supplementary material was added later, after a different reviewer requested an additional experiment.

9. Line 113: which load? Similar or higher than experimental load? If similar or lower, than there is a possibility that in the beginning of the experiment there will be significant grain rearrangement, leading to fast initial compaction (c.f. Pluymakers et al., 2014). You should be able to determine if this was significant by comparing the scan made at the reference point versus the one made at  $t=1$ . Did you determine the porosity in the reference scan? If so, nice to mention here.

The load to pre-compact the samples was similar to the experimental load. We followed the procedure described in Spiers et al. (1990). The pure NaCl sample exhibited an initial porosity of ~36%, while the sample with biotite, due to the different grain packing and an initial different height, exhibited a porosity of ~33%. We interpret grain rearrangements and fast dissolution rates at small contact areas to be the cause of the initial fast compaction (lines 371-372). We have amended the text accordingly (lines 100-101).

10. Line 120: 3 significant numbers, how precise is this load controlled? Really  $6.64 \pm 0.01$  MPa? Was the sample unloaded to make the scans?

Please see our reply in the previous rebuttal The load was kept constant between 6.4 and 6.6 MPa for the duration of the experiment. The samples needed to be unloaded to allow for scan acquisition.

11. Line 127/Fig 2: Fig 2 indicates 11 datasets

That is true, but the first reference scan (0) is not numbered in the figure, thus the experiment led to 12 datasets. We have clarified this in the figure caption.

12. Line 139: Include here if the initial height of the sample is taken from the reference scan, after pre-compaction. (same as line 102)

The text has been revised to include the reviewer's suggestions.

13. Line 146: figures 1-2-3 are not labelled in order, or did I miss figure 3?

Figure numbering now follows the order of their appearance in the manuscript text.

14. Fig 4/line 102-103: in fig 4 initial porosities are 0.36 and 0.33, and in line 102-103 this is 0.39 and 0.33. Is this a difference between for and after pre-compaction?

The reviewer identified a mistake in our reporting of the values in the text. Line 102 has now been modified to include the correct value.

15. Line 130: you need a list somewhere indicating at which time the scans were taken, or you need to indicate in all your figures at which scan-point they are taken. Now it is pretty difficult to relate Figure 4 with Figure 2 - when is 22.5 hours? 208 (V I assume?) and 2455 (XI I assume?) are a bit easier to guess. This also goes for following figures.

A list has been added to the Supplementary Info to indicate at which time the scans were taken, and to which amount of vertical shortening they correspond (Table S2). This list is being referred to in the main text.

16. Line 182: so strain rate was  $[d\langle\epsilon\rangle(t) - d\langle\epsilon\rangle(t_0)]/t(t)$ ? Or  $[d\langle\epsilon\rangle(t) - d\langle\epsilon\rangle(t-1)]/[t(t)-t(t-1)]$  If the latter, shouldn't the strain rate for NaCl between VIII and IX be negative?

The values of strain/pixel (derived from the DVC analyses) were divided by the time (in seconds) between each pair of correlated images using the mathematical operation functions available in ImageJ. This operation yields the integrated strain rates ( $s^{-1}$ ) for each point in the sample over the given time interval. This analysis returns the local strain rates, and not the bulk strain rates (as reported in Fig. 2b, for which negative values have indeed been calculated between VIII and IX compaction step).

17. Line 211: 'microfracturing' This is scale dependent, any microfractures would need an aperture of at least 2x voxel size in order to be visible, which means apertures of 12-13 micrometer at least. That is quite a bit...

We agree with the reviewer's comment, and we modified the text accordingly. We wanted to highlight that no microfracture indicative of brittle deformation could be resolved.

18. Fig. 5: the figure might be easier to grasp if you would plot strain rate instead of strain in this plot, but up to authors. The text clarifies sufficiently.

As the reviewer is happy with the text clarification, we decided to keep the figure as it is.

19. Line 250-266: 15 lines on a figure in the supplement, whereas Fig. 1 is mentioned once. This seems out of balance, consider swapping Figures, or shorten the description of this figure (i.e. only line 250-253, + line 265 for example?)

We revised the text to improve clarity and balance in the description.

20. Fig 7: why didn't you circle all areas of local compaction? What makes the one in the white circle special? Good improvement of Figs 7 and 8 by the way!

The circles are examples of areas showing highest compaction/strain localisation. Highlighting all areas of compaction with circles would have rendered the figure too cluttered and unclear.

21. Line 285-295: any opinion on the local dilation in volumetric strain? Real or artefacts? If real, any idea what they mean?

We speculate that the local dilation areas in the volumetric strain represent local redistribution of grains and changing pore geometries, while the compaction values represent the real compaction and local porosity reduction. We believe that the dilating volumes are indeed real and not artefacts.

22. Line 301: why give first order of magnitude, then  $3 \times 10^{-8}$ ? Looks odd

The text has been improved for clarity.

23. Caption to Fig 9: include what the holes mean.

We modified the caption accordingly.

24. Line 325: the shapes of the curves together with your microstructures forms indeed convincing evidence of PS. Why not include the microstructures in the sentences here?

We agree that the combination of evidence from our compaction curves and from microstructures is convincing evidence of PS. However, in this case, we consider that the existing structure maintains clarity and more effectively guides the reader through our observations and interpretation.

25. Line 331: what was similar in the behaviour, the shape of strain vs time? The absolute rates? With the coarse grains here one would expect interface-controlled PS. In the studies used for comparison here (Renard and Spiers) grains are smaller and stresses were different. Are they nevertheless also expected/proven to be interface-control?

We compared the time-evolution of strain in their data with the one from our data. In these previous studies, the authors observed a very steep initial gradient, as in our data, and similar vertical shortening amounts. In NaCl, kinetics is known to be transport/(diffusion)-controlled (Spiers and Brzesowsky, 1993), while in fine-grained water-saturated quartz compounds the kinetics are known to be interface-controlled (Lehner and Bataille, 1984). We therefore do not feel that the kinetics in the studies presented by Renard or Spiers should be interface-controlled.

26. Line 330-344: a bit unsure what you are trying to say in this paragraph. The first part of the paragraph is on the effects of clay on compaction behaviour, without a conclusion (line 330-340). In Renard et al the increased compaction was explained with the inactive clay propping open the fluid pathways. In your sample this can't be the reason. In the second part (line 340-344) compares to Spiers et al, 1990, which is pure NaCl. Looking at their paper, Fig 5, they show for a grain size comparable to yours ( $275 \pm 25 \mu\text{m}$ ) volumetric strain rates of  $8 \times 10^{-4}$  to  $10^{-7}$ . Your vertical strain rates for the pure NaCl sample are  $10^{-6}$  to  $10^{-8}$  (Fig 2); and the volumetric strain rates from DIC are  $10^{-6}$  to  $10^{-7}$  (Fig 9). Spiers et al have a lower effective stress, so theoretically their strain rates should be lower than yours. Can you explain this discrepancy?

Our study explores the time evolution beyond the initial steep compaction rate shown in Renard et al. (2004) and Spiers et al. (1990) and provide a visual assessment of the spatial distribution of local strain rates. However, after  $\sim 7$  days of deformation, Spiers et al. (1990) reached 20 % vertical shortening (Fig. 3): over that time interval, the integrated bulk strain rates are  $\sim 10^{-7} \text{ s}^{-1}$ , for comparable grain sizes (Fig. 5). In the same time interval, our data show comparable integrated bulk strain rates (Fig. 2b). However, in longer interval times (later in the experiment), our data progressively show lower integrated bulk strain rates. The volumetric strain rates reflect the local distribution of strains within the sample for each time interval between correlated images. At the very beginning, our pure NaCl data shows similar values to Spiers et al., (1990). It is only later on, with more deformation, that lower strain values are obtained. Initial packing and porosity content are likely to affect the overall gradual vertical shortening and have an effect on the bulk strain rates.

The text has been revised to improve clarity.

27. Line 348: after 400 hours you only have 3 datapoints, which seem too have an error of about half the symbol size (comparing VII and VII for example). For me, that would make it difficult to attach strong conclusions to estimate if the trend is linear or constantly decelerating (the latter is what is predicted by PS theory).

We agree with the reviewer, and we modified the text line accordingly.

28. Line 349: indeed a plausible explanation

29. Line 369-382: I am still not convinced about these force chains. In which image would they be visible? Can you indicate them somewhere? I do not see them in Figs 7 or 9. The only clear 'chains' I see are in the NaCl/bio sample in Fig 9, and are formed and explained by the presence of the biotite flakes, which speed up the compaction rates.

We envisage the force chains to be dynamic and to change relatively quickly over time. A careful visual assessment of the maxima of the DVC results in the pure NaCl sample showed how these maxima are transient and how they change positions between pairs of correlated images. To help the reviewer visualising them though, we created a new figure 3, in which an overlay of what we interpret to be *force chains* has been added to the  $\mu$ CT images. This figure has now been included in the Supplementary Material (Fig. S8). However, we do not believe these "outlines" to illustrate definite force chains, as force chains are 3D features. The dynamic force chain model is, at this stage, a speculative one which plausibly explains some of our findings. It remains for further (ongoing) studies to test it.



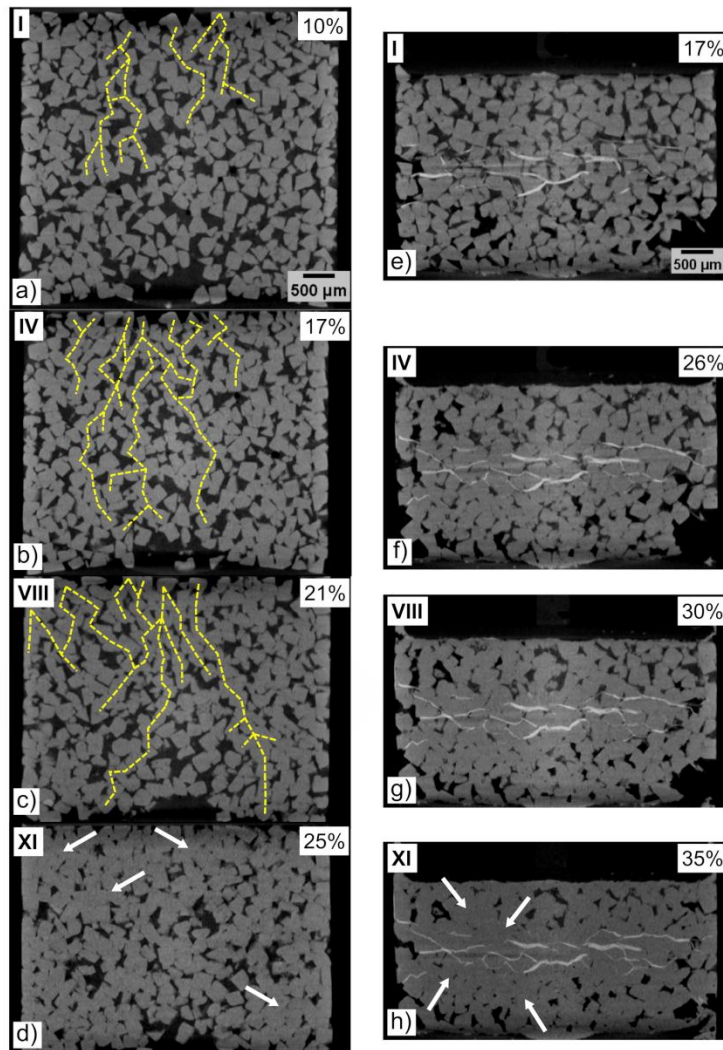


**Figure S8** The yellow traced lines estimate the location of *dynamic force chains*, on top of Fig. 3.

30. Line 383-392: is the higher chemical potential a different or a similar explanation from the faster ion exchange? Unclear from this text. Wrt ion exchange, I am a bit confused, given that for PS you also need precipitation. If there is no mechanism liberating Cl, where does the Cl then come from to precipitate extra NaCl? Or are you proposing the NaCl completely dissolves?

The ion exchange hypothesis is a different explanation from the chemical gradient between dissimilar phases. This process would be strongly limited by the ion exchange site availability. The *ion activity product*,  $\{Na^+\} \cdot \{Cl^-\}$ , must equal the *solubility product constant*  $K_{sp}$  for NaCl, but  $Na^+$  needs not to be equal to  $Cl^-$ . Consequently, any rise in  $Na^+$  through an ion exchange process, maintaining charge balance, would increase the ion activity product (which is assumed initially to be in equilibrium with NaCl) and cause NaCl to form. Conversely, removal of either  $Na^+$  or  $Cl^-$  via ion exchange would achieve dissolution. Because the biotite flakes are large, the surface area is reduced and therefore the sites may be limited, contributing relatively small to the process. We therefore modified the text accordingly by discarding this hypothesis.



31. Line 396-403: the grain shape is actually odd: from a shape perspective, the extreme reduction in porosity in the biotite layer is actually odd: there is practically insoluble biotite forming a large planar surface, and then the NaCl cubes make initially a sharp contact. However, already in the first step the contact areas of NaCl against biotite are huge (Figure 8a) compared to the NaCl-NaCl contacts. So whatever makes it speed up, is relatively speaking a stronger driving force than the contact stress, since these must be low in this zone. Or are you proposing that the biotite flakes have an irregular surface (i.e. by the reference to Pluymakers and Spiers)?

We are not proposing that the biotite flakes have irregular surfaces. Rather we propose that initially the geometric arrangement of the grain contacts between a cube and a plate-like mineral may create 'asperities', with lower contact areas, which could have assisted the driving force of the mechanism. With increasing deformation these contacts became progressively smoother and possibly contribute to slow down in the compaction from 400 hours onwards. However, we believe that the chemical potential gradient between dissimilar phases is the main mechanism for the initial fast compaction rates in this sample and it explains the initial DVC local strain rates. The text has been modified to improve clarity (lines 381-385).

32. Line 422: which additional salt? The one from the fast ion exchange?

Our analyses – compaction curves vs porosity evolution – evidence that compaction correlates to porosity reduction, which means that some mechanism other than pore collapse must be responsible for the porosity reduction. In the absence of compaction, this can only be the filling of pores by precipitated salt. We are implying that NaCl from the marginal pure NaCl layers is dissolved, transported and reprecipitated in the central biotite-bearing layer, following Merino's textural model.

33. Line 429: again, where? Can you indicate a specific location?

34. Line 431: Where? Can you indicate a specific location?

The areas where salt has been reprecipitated into the biotite-layer are the areas with reduced porosity and higher grain impingements, essentially the same areas circled in Fig. 3.

35. Line 421-431: as the comment above: I like this theory, but it can be integrated a bit better with the preceding hypotheses. What is the role of each possibility, and in which part of the experiment do they play a role?

The time intervals at which each hypothesis plays a role in the experiment is outlined in the text (lines 383-386, 408 and added line 425). Along these lines, references to the figures have been included to help the readers following the discussion, and we therefore feel that there is enough cross-referencing within the text. The hypothesis outlined in lines 421-431 are only a summary of what is discussed beforehand. We provide a brief summary below:

- 0-150 hours: enhanced dissolution by chemical potential driven by different phases and initial compaction of biotite layer; this caused the biotite-bearing layer to compact, and porosity to reduce in this layer. This also caused the initial steep vertical shortening of the sample;
- 150 - 400 hours: the compaction of the biotite layer induced an increase of the contact areas, lowering the stresses at local points. It also increased dissolution in smaller contact,

higher stress areas located at the marginal salt layers. However, with increasing shortening, the contact areas in the NaCl layer increased, which lowered the stresses at contact points and, as a consequence reduced the driving force for PSC (line 408).

- 400 hours onwards: Porosity reduction in the biotite layer is accommodated by enhanced salt deposition, which lowers the driving force for PSC and slows down the process.

36. Section 4.2: given what you now have observed on the effect of the biotite flakes, do you then think stylolites can only form in rocks with a similar irregularity?

Our results show that biotite flakes contribute to reduce porosity and pore connectivity, and to increase the local strain rates as compared to neighbouring pure salt layers. It is evident from our results how biotite flakes contribute to reduce porosity and pore connectivity, and increase the local strain rates. However, at the same time, they do not seem to facilitate strain localisation (i.e. bulk compaction rates are virtually unchanged). We believe that enhanced pressure-solution is locally caused by a chemical potential driven by dissimilar phases. The effects of particle shapes, size as well as phyllosilicate types remain unclear. These are effects which we would like to explore in future studies, to integrate the current knowledge and provide a better understanding of the pressure-solution process and stylolite nucleation/growth.

### List of changes

Line 20: "...The results show that **for mixed samples (NaCl+biotite)**, ~~in NaCl~~, phyllosilicates induce a marked..".

Line 44: "...(e.g. Aharonov and Katsman, 2009; Angevine and Turcotte, 1983; Bos et al., 2000; Croizé et al.,...)"

Line 46: " These alterations, **may**, in turn,..".

Line 75-80: "**We use NaCl aggregates as analogues for geomaterials and sedimentary rocks undergoing PSC.** Previous compaction experiments have demonstrated that NaCl samples deform sufficiently quickly to enable the study of PSC in a laboratory environment at room temperature (Gratier, 1993; Renard et al., 2004, 2001; Schutjens and Spiers, 1999; Spiers et al., 1990). ~~Despite being geomaterials in their own right, in this study, we use NaCl aggregates as analogues for sedimentary rocks undergoing PSC.~~"

Line 99-103: "grains clogging the fluid connections and both samples were saturated with NaCl solution. Initial porosity of the two sample compositions has been calculated from mass of the salt quantitatively added and the dimensions of the initial salt **reference** stack. The pure NaCl sample exhibits an initial porosity of **~36%**, while the sample with biotite, due to the different grain packing and an initial different height (**5 mm in NaCl vs 3.7 mm in NaCl-biotite**), exhibits a porosity of **~33%**."

Line 120: "...uniaxial stress of **6.4 to 6.6 MPa** MPa."

Line 140: "...where  $x_0$  represents the initial height of the sample (**measured from the reference scans**), and.."

Line 212: “..action of **cataclasis**, nor indented grains to have formed in the first 100 hours.”

Line 254-257: “contributed relatively small amounts to the total pore volume (Supplementary Fig. S5c). Similar observations were made in the NaCl-biotite sample. ~~In the subvolume, the number of small pores (volume < 2.6 x 10<sup>5</sup> μm<sup>3</sup>) increased from 477 to 664 with increasing deformation (Supplementary Fig. S5b), while the largest pores (volumes > 2.6 x 10<sup>5</sup> μm<sup>3</sup>) showed more than a twofold decrease.”~~

Line 264-265: “large pores (Supplementary Fig. S6b). ~~Overall, the number of pores decreased from 1144 to 562 over the duration of the experiment.”~~

Line 300: “10<sup>-6</sup> – 10<sup>-7</sup> to ~~3 x~~ 10<sup>-8</sup> – 10<sup>-9</sup> s<sup>-1</sup>, whereas volumetric strain rates decreased from -10<sup>-6</sup> to -10<sup>-8</sup> s<sup>-1</sup> in...”.

Line 329: “Earlier, shorter studies by Renard et al. (~~2001~~, 2004) and Spiers et al. (1990) showed a very similar...”.

Line 334-342: “~~They concluded that the presence of clays favours grain contact healing, reducing porosity and favouring pressure-solution creep. In Renard et al. (2001), mixtures of salt and clays were loaded for 15 days under different loads (0.1, 0.5 and 4 MPa). Smaller grain sizes were used: NaCl was sieved between 106 and 250 μm, while a pottery bentonite was used and sieved between one and five μm. Their results showed how the presence of small clay particles significantly enhanced the compaction rate over time.~~ Spiers et al. (1990) performed tests on brine-saturated NaCl powder (grain size 100-275 μm) at temperatures of 20-90°C and applied stresses of 0.5-2.2 MPa, testing theoretically-derived constitutive equations. ~~For similar grain sizes and time interval, their results showed similar orders of bulk strain rates.~~ “

Line 351: “The ~~non-linear~~ decrease in the...”.

Line 382: “chains in the pure NaCl layers (Supplementary Fig. S8).”

Line 386-394: “~~Fast exchange of K<sup>+</sup> and Na<sup>+</sup> has been observed between biotite grains and NaCl saturated solutions (Reed and Scott, 1962; Scott and Smith, 2013) and might have been relevant in our experiments (Bray et al., 2014; Hu et al., 2013). It is possible that in our experiments a faster ion exchange occurred between K<sup>+</sup> in the biotite and Na<sup>+</sup> in the NaCl solution, making the NaCl solution undersaturated in Na<sup>+</sup> and enriched in K<sup>+</sup> over time. This would cause more dissolution of Na<sup>+</sup> from NaCl grains and transport of ions in solution, and material to precipitate in nearby pores. This mechanism would explain the reduced porosity within the NaCl biotite layer. While this mechanism probably does not account solely for the localization of PSC around biotite grains, it could have contributed.~~”

Line 395-398: “The initial geometric arrangement of the grain contacts between a cube and a plate-like mineral (i.e. salt vs biotite) may create ‘asperities’, with lower contact areas, which could assist the driving force of the mechanism. From 400 hours onward, the process might have slowed down because reduced porosity was met by reduced asperities/irregularities in the grains, which became progressively smoother as compaction progressed (lower contact stresses). We envisage that these mechanisms contributed to pressure solution.”

Line 424-425: “From 400 hours onwards, the removal of dissolved material leaves less material to carry the load...”.

Overall, the text has been revised to improve clarity.

**Highlights:**

- Local porosity around biotite grains is reduced by ~100 % during pressure-solution;
- Biotite increases the local strain rates by an order of magnitude;
- Pressure-solution is enhanced due to geochemical self-organization.

1 4D porosity evolution during pressure-solution of NaCl in the presence  
2 of phyllosilicates

3

4 **Alice Macente**<sup>a,1</sup>, Florian Fousseis<sup>a</sup>, Ian B. Butler<sup>a</sup>, Erika Tudisco<sup>b</sup>, Stephen A. Hall<sup>c</sup>, Edward Andò<sup>d</sup>

5 <sup>a</sup> University of Edinburgh, School of Geosciences, The King's Buildings, James Hutton Road,  
6 Edinburgh EH9 3FE

7 <sup>b</sup> Lund University, Division of Geotechnical Engineering, John Ericssons väg 1, Lund, Sweden

8 <sup>c</sup> Lund University, Department of Solid Mechanics, Ole Römers väg 1, 223 63 Lund, Sweden

9 <sup>d</sup> Univ. Grenoble Alpes, CNRS, Grenoble INP<sup>2</sup>, 3SR, F-38000 Grenoble, France

10 Corresponding author: Alice Macente

11 Corresponding author's email: [alice.macente@gmail.com](mailto:alice.macente@gmail.com)

12

<sup>1</sup> Stanford University, Department of Geophysics, 397 Panama Mall, Stanford, CA 94305

<sup>2</sup> Institute of Engineering Univ. Grenoble Alpes

13 **Abstract**

14 Pressure-solution creep is one of the most common crustal deformation mechanisms, inducing  
15 changes in the porosity and permeability of rocks. For a variety of rock types undergoing  
16 pressure solution, it has been shown that the presence of phyllosilicates may significantly  
17 enhance the rate of the pressure-solution process. In this experimental investigation, we  
18 present 4-dimensional (three dimensions + time) X-ray microtomographic data that contrast  
19 deformation by pressure-solution of a pure NaCl aggregate with that of a mixture of NaCl and  
20 biotite. The results show that for mixed samples (NaCl+biotite), phyllosilicates induce a marked  
21 reduction in porosity and pore connectivity and contribute to an increase in the local strain  
22 rates by an order of magnitude over pure NaCl samples. At the same time, phyllosilicates do not  
23 induce strain localization in the sample. We discuss various possible explanations for these  
24 observations including a possible positive feedback between the porosity distribution and  
25 pressure solution. Our study yields novel insights into the local effects of phyllosilicates during  
26 pressure-solution creep and provides full 4-dimensional imaging and characterization of the  
27 coupled evolution of porosity and pore connectivity over previously unprecedented  
28 experimental time scales.

29

30 **Keywords (6):** pressure-solution creep; phyllosilicates; X-ray microtomography; Digital Volume  
31 Correlation; geochemical self-organization;

32



33 **1. INTRODUCTION**

34 Pressure-solution creep (PSC) is one of the key mechanisms of fluid-rock interaction and  
35 can induce significant changes in the transport properties and the composition of rocks. A wide  
36 range of geoscience applications, including hydrocarbon extraction, CO<sub>2</sub> storage and  
37 geothermal energy harvesting from hot sedimentary aquifers, rely on an accurate knowledge of  
38 the porosity and permeability of reservoir rocks. Understanding how these properties are  
39 affected by PSC is therefore of crucial importance.

40 PSC is a solution mass transfer process in response to the application of non-hydrostatic  
41 stresses that involves (i) dissolution at stressed contact points, (ii) mass transport through a  
42 fluid phase along grain boundaries, and (iii) re-precipitation of the dissolved material in the  
43 nearby low-stress areas (pores, veins) (Gratier et al., 2013; Rutter, 1983). PSC induces changes  
44 in the microstructure, pore structure, composition and strength of a wide range of geological  
45 materials (e.g. Aharonov and Katsman, 2009; Angevine and Turcotte, 1983; Bos et al., 2000;  
46 Croizé et al., 2010; Gratier, 1993; Gratier et al., 2005; Hickman and Evans, 1995, 1991; Lehner  
47 and Leroy, 2004; Pluymakers and Spiers, 2015). These alterations may, in turn, affect the  
48 transport properties of rocks (Sprunt and Nur, 1977, 1976). PSC has also been observed to  
49 trigger strain localization leading to the formation of stylolites (Gratier, 2003; Gratier et al.,  
50 2013;). Strain localisation during PSC has been recognized as involving feedbacks between  
51 solution/precipitation reactions and an evolving pore structure and thus a coupling between  
52 chemical, mechanical and hydraulic processes (Merino et al., 1983; Ortoleva et al., 1987).

53 While the effects of PSC on transport properties have been investigated extensively in a  
54 wide range of rocks (see Gratier et al. (2013), and references therein), the dynamic evolution of

55 these coupled processes at the grain scale remains poorly understood. This is primarily caused  
56 by the previously limited possibilities to image PSC in three dimensions over time. Renard et al.  
57 (2004) were the first to use 4-dimensional (4D, three spatial dimensions and time) synchrotron-  
58 based X-ray microtomography ( $\mu$ CT) to study the effects of PSC during compaction of pure NaCl  
59 aggregates. They imaged the reduced pore space and the impingement of grain contacts and  
60 inferred that the mean permeability in their samples decreased dramatically during  
61 compaction. Despite its pioneering character, this study did not explore PSC in the presence of  
62 phyllosilicates, which have been shown to hold the potential to significantly affect the rate of  
63 PSC (Aharonov and Katsman, 2009; Bos and Spiers, 2002; Hickman and Evans, 1995; Renard et  
64 al., 1997). Here we present 4D X-ray microtomographic data that contrast the deformation of a  
65 pure NaCl aggregate by PSC with that of a mixture of NaCl and biotite, in order to investigate  
66 the effects of phyllosilicates on the progressive shortening and the concomitant evolution of  
67 porosity and pore connectivity of the samples. The combination of  $\mu$ CT with *Digital Volume*  
68 *Correlation* (DVC, e.g. Andò et al., 2012; Tudisco et al., 2017) enables quantification of strain  
69 and strain rates at the grain scale and following of the evolution of these parameters during  
70 sample compaction. Our findings suggest that in NaCl aggregates: i) bulk porosity and pore  
71 connectivity are critically reduced in the presence of phyllosilicates; ii) phyllosilicates contribute  
72 to increase the strain rates achieved by PSC by an order of magnitude with respect to the  
73 monomineralic NaCl domains.

74

## 75 **2. MATERIAL AND METHODS**

### 76 **2.1 Introduction**

77 We use NaCl aggregates as analogues for geomaterials and sedimentary rocks undergoing  
78 PSC. Previous compaction experiments have demonstrated that NaCl samples deform  
79 sufficiently quickly to enable the study of PSC in a laboratory environment at room temperature  
80 (Gratier, 1993; Renard et al., 2004, 2001; Schutjens and Spiers, 1999; Spiers et al., 1990).

## 81 **2.2 Materials**

### 82 **2.2.1 Sample Preparation**

83 Two different samples were prepared in x-ray transparent uniaxial presses (see section  
84 2.2.2) to test the effect of different sample compositions on PSC. The total sample mass was  
85 chosen to produce cylindrical samples with diameters of 5 mm and an initial height of ~5 mm.  
86 For the first sample, granular NaCl (analytical reagent, Fisher Scientific) was sieved to a 250-300  
87  $\mu\text{m}$  grain size. This sample acted as our monomineralic reference. The second sample consisted  
88 of a mixture of NaCl and biotite grains at a ratio, by mass, of 4:1. The NaCl was sieved to give  
89 the same grain size as the first sample. Biotite flakes with grain sizes between 212 and 750  $\mu\text{m}$   
90 (longest dimension) were obtained by cutting mica sheets from a biotite single crystal using a  
91 scalpel. Biotite was chosen because of the contrast in X-ray absorption with respect to NaCl; in  
92  $\mu\text{CT}$  data biotite flakes appears as bright grains, NaCl appears as light grey grains, while (brine-  
93 filled) pores are dark grey (Fig. 1). In the press, the NaCl/biotite mixture (1.4 mm thick) was  
94 confined by two pure NaCl layers (0.95 mm top layer, 1.27 mm bottom layer). In this way, the  
95 two pure NaCl layers constitute a 'reference' material within the sample to compare the degree  
96 of compaction under the same experimental conditions. The materials were introduced into the  
97 presses sequentially as slurries. Biotite within the central layer showed no preferential  
98 alignment prior to compaction. In each of the two samples, two discs of filter paper were

99 placed above and below of the samples, to avoid grains clogging the fluid connections. Both  
100 samples were saturated with NaCl solution. The initial porosity of the two sample compositions  
101 has been calculated from the mass of the salt quantitatively added and the dimensions of the  
102 initial salt reference stack. The pure NaCl sample exhibits an initial porosity of ~36%, while the  
103 sample with biotite, due to the different grain packing and an initial different height (5 mm in  
104 NaCl vs 3.7 mm in NaCl-biotite), exhibits a porosity of ~33%.

### 105 **2.2.2. Experimental Setup**

106 The samples were compacted in X-ray transparent presses. These experimental presses  
107 were built in-house and comprise a 5 mm diameter cylindrical piston that was fashioned to be a  
108 close running-fit to the lower cylindrical sample chamber (Supplementary Fig. S3). The cells  
109 were manufactured from PEEK (Polyether-ether-ketone). Loading frames, composed of two 20  
110 mm thick Perspex plates joined by three threaded rods, allowed a pneumatic actuator to apply  
111 a constant uniaxial load on the samples. The close running-fit of the piston enabled a narrow  
112 annulus of high-vacuum silicone grease to be used to provide a fluid seal between the piston  
113 and sample chamber.

114 Initial loading of the sample using the pneumatic actuator for 10 minutes was used to  
115 produce a pre-compacted starting material. At this stage, a reference  $\mu$ CT scan was acquired  
116 (see section 2.2.3). Subsequently, the inlet and outlet tubes to the cell, as well as the sample,  
117 were flushed with a pre-saturated NaCl solution to ensure that no air bubbles remained in the  
118 system, enabling the experiments to start saturated with brine. To maintain fluid saturation, a  
119 pre-saturated NaCl solution filled reservoir attached to the lower fluid inlet of the cell was

120 mounted ~40 cm above the cells (Supplementary Fig. S3). The sample was then loaded to a  
121 constant uniaxial stress which was stable between 6.4 and 6.6 MPa.

### 122 **2.2.3 Image Acquisition**

123 During each experiment, 3D  $\mu$ CT data were acquired using the custom-built  
124 microtomograph in the School of Geosciences, at the University of Edinburgh (see Cnudde and  
125 Boone (2013), for the fundamentals of laboratory X-ray  $\mu$ CT and Table S1 for data acquisition  
126 parameters). Combined, the data acquired during the experiments formed a 3D time series, i.e.  
127 4D datasets. Compaction was interrupted for scanning of the samples. For each sample, twelve  
128  $\mu$ CT datasets were acquired over 2455 hours of compaction (Fig. 2, 3, Table S2), allowing  
129 monitoring of the evolution of porosity and grain morphologies over time. Initially, the samples  
130 were scanned in short time intervals (2, 4, 6 hours), to monitor the mechanical behaviour of the  
131 samples, and capture relatively rapid initial deformation. Successively, the time interval  
132 between each scan was increased to monitor the progressively slower deformation of the  
133 sample (Table S2).

### 134 **2.2.4 Image Processing**

135 The  $\mu$ CT data were reconstructed using Octopus<sup>®</sup> software (Dierick et al., 2004) yielding  
136 a voxel (3-dimensional pixel) volume of  $6.5^3 \mu\text{m}^3$ . The twelve microtomographic volumes  
137 acquired for each deformation experiment were analysed individually, to assess sample  
138 compaction and to measure the evolution of porosity and pore connectivity. The height of the  
139 samples in between the top piston and the bottom of the cell was measured from the vertical  
140 slices through each  $\mu$ CT scan, and the relative shortening was calculated through

$$\varepsilon_t = \frac{x_0 - x_t}{x_0}$$

141 where  $x_0$  represents the initial height of the sample (measured from the reference scans), and  
142  $x_t$  represents the height at a given time  $t$ . The  $\mu$ CT datasets were denoised using a *median filter*  
143 with a kernel size 2. Subvolumes of dimensions  $400^3$  voxels, equivalent to a cube of  $17.6 \text{ mm}^3$   
144 (i.e., 2.6 mm on each side), were cropped from the central regions of the reconstructed  $\mu$ CT  
145 volumes to conduct porosity analyses and avoid artefacts from the cell boundaries. The  
146 workflow, applied in AvizoFire® v. 8 and Avizo® v. 9, is detailed in Supplementary Figure S4. The  
147 pore space was segmented by the application of an *interactive threshold* to produce binarised  
148 image stacks from which the total porosity was determined using the *volume fraction* operator  
149 (Arns et al., 2002) (Fig. 4a). The sensitivity of the segmentation and interconnectivity analysis to  
150 changes in the threshold values was established by repeating the procedure on volumes that  
151 were eroded and dilated by one voxel (see Füsseis et al. (2012) and Macente et al. (2017) for  
152 details of the analysis). This procedure yielded error bars on the porosity measurements. Slice-  
153 by-slice (2-dimensional) porosity analyses were also performed to determine the evolution of  
154 the porosity along the direction of loading (Fig. 4b, c, d).

155 Pore space connectivity was characterized in the segmented data using the *label*  
156 function and a voxel coordination value of six, where the *labeling* operator identifies  
157 neighbouring voxels that share a cube face and assigns them to an individual pore cluster (Fig.  
158 5, 6). From these clusters, individual pores were separated using the *Separate Objects* operator  
159 with a coordination number of six, and a marker extent equal to one (least connected objects).  
160 Separation points represent pore throats. Subsequently, the individual pores were analysed for  
161 their volume in the individual datasets using the *Label analysis* operator. The smallest pores  
162 considered in the pore size distribution analyses were 10 voxels in volume, or  $2.7 \times 10^3 \text{ }\mu\text{m}^3$ .

163 We treated the central mixed layer and the marginal pure NaCl layers in the NaCl-biotite  
164 sample as three discrete subdomains in order to assess and compare their relative evolution.  
165 From the  $400^3$  voxels subvolumes, these subdomains were extracted using the *Extract volume*  
166 operator in Avizo, by identifying where the biotite flakes first occur and end vertically along the  
167 sample. The marginal NaCl layers were also compared with the pure NaCl sample.

### 168 **2.3 Digital Volume Correlation (DVC)**

169 Digital Volume Correlation (DVC) was used to measure the local distribution of  
170 displacements (from which maximum shear strains and volumetric strains are obtained) in the  
171 sample between two successive time steps (see Supplementary Material for details on the  
172 technique). DVC, which spatially resolves displacements with a sub-voxel accuracy, was  
173 performed on consecutive pairs of  $\mu$ CT 3D datasets using the code *TomoWarp2* (Tudisco et al.,  
174 2017) and computed on the Edinburgh Compute and Data Facility's Terracorelator cluster  
175 (Atkinson et al., 2015). Results were visualized in the open-source software Fiji (Schindelin et  
176 al., 2012). Misalignments in x and y, and misorientation in excess of  $5^\circ$  between the two 3D  
177 datasets can introduce errors in the outputs of the correlation and needed to be corrected. Two  
178 small markers at the base of the experimental cells were used together with the central fluid  
179 bore in the press to define the position and orientation of the datasets to enable the correction  
180 of misalignments and misorientations between two subsequently acquired time steps using the  
181 *rotate* and *translate* operators in Fiji. Figures 7 and 8 show the 3-dimensional results of DVC  
182 represented by XZ vertical slices through the middle of the analysis volumes for progressively  
183 shortened datasets. Absolute strain-rate values were calculated by dividing the DVC strains by  
184 the duration of loading (in seconds) between each analysed  $\mu$ CT scan (Fig. 9).



## 185 **2.4 Scanning electron microscopy**

186           Secondary electron images were acquired after the deformation experiments to study  
187 the grain-scale effects of pressure solution in the sample. Before retrieving the samples, the  
188 brine was displaced using compressed air. The samples were then retrieved from the uniaxial  
189 cells and portions of the samples carefully extracted. This procedure may introduce physical  
190 damage to the sample microstructures. For this reason, we only investigated evidence for PSC  
191 (i.e. indented grains, suture zones) in areas that were ‘undisturbed’ and represented  
192 consolidated portions of the original samples. Gold coated samples were imaged using a Carl  
193 Zeiss SIGMA HD VP Field Emission SEM with an acceleration voltage of 10 kV. Samples were  
194 mounted on an aluminium stub using a self-adhesive conducting pad prior to gold coating.

## 195 **3. RESULTS**

### 196 **3.1 Bulk deformation**

197           The measurements of vertical shortening show that the *pure NaCl* sample shortened a  
198 total of 25 % over 2455 hours of compaction. The compaction curve was initially steep, where  
199 the sample accommodated 10 % vertical shortening in 22.5 hours. Between 155 and 255 hours,  
200 the compaction rate slowed down. Beyond 400 hours of compaction, the gradient of the curve  
201 did not change substantially and we consider the sample to deform in steady state there (Fig.  
202 2a). The compaction curve for the *NaCl-biotite* sample displays an identical pattern. However,  
203 the sample reached a total of 35 % vertical shortening at the end of the experiment, with very  
204 fast shortening of ~17 % in the first 22.5 hours. Compaction decelerated over the same time  
205 interval as the pure NaCl sample, again reaching what appears to be a steady state  
206 deformation. In both experiments, compaction was still ongoing at the end of the experiment.

207           These trends are reflected by the evolution of bulk strain rates over time (Fig. 2b). The  
208 data showed an immediate decrease in bulk strain rates after initial compaction. Some  
209 differences were present between 208 and 376 hours of compaction, when the two samples  
210 deformed less over a significant time period, resulting in lower strain rates (Fig. 2b).

211           Inspection of vertically centred slices through the  $\mu$ CT data revealed some key  
212 differences between the two samples (Fig. 3). The NaCl sample showed no microstructures  
213 indicative of the action of cataclasis, nor indented grains to have formed in the first 100 hours.  
214 However, after some compaction, porosity was reduced and grains started to agglomerate (Fig.  
215 3c, d). In the NaCl-biotite sample, the porosity reduction was localised in the biotite-bearing  
216 layer early on (Fig. 3f). In this layer, NaCl grains lost their cubic habit with increasing  
217 compaction. Biotite generally showed a progressive alignment in the direction perpendicular to  
218 the loading, although some grains were trapped in their orientation and left without room to  
219 move (Fig. 3 e-h, centre bottom). In comparison, the marginal NaCl layers developed fewer  
220 NaCl grain impingements, and  $\sim 10\%$  of porosity remained after 2455 hours of compaction.  
221 These observations mirrored those from the pure NaCl sample.

222

## 223 **3.2 Porosity evolution**

### 224 **3.2.1 Bulk Porosity**

225           We analyzed the distribution of porosity change during compaction in the cropped  
226 subvolumes to identify any heterogeneities that could be indicative of strain localization in our  
227 samples and to evaluate the evolving transport properties (Fig. 4a). In the case of the pure NaCl  
228 sample, as compaction proceeded the bulk porosity was reduced from 36 to  $\sim 13\%$  (Fig. 4a).

229 Slice-by-slice porosity measurements along the vertical axis of the sample (Z-direction) confirm  
230 that this porosity reduction was evenly distributed in the sample and that no strain localization  
231 had taken place (Fig. 4b, c, d). The upper portion of the sample showed a slightly larger  
232 decrease in porosity as compared to the rest of the sample. In the case of NaCl-biotite sample,  
233 bulk porosity decreased by ~25 % over the duration of the experiment (Fig. 4a). The slice-by-  
234 slice analysis shows that at some vertical positions porosity decreased to 0 % after 2465 hours  
235 of compaction (Fig. 4d).

236 To better illustrate the effect of sample composition, shortening was evaluated  
237 separately for the biotite-bearing layer and the marginal NaCl layers of this sample (Fig. 5). The  
238 marginal NaCl-bearing layers were combined in the analysis. Essentially, shortening was  
239 accommodated to roughly equal parts by all three layers. The biotite-bearing layer shortened  
240 marginally more (36 %), with its thickness decreasing from 1.4 mm to 0.9 mm over 2455 hours  
241 (Fig. 5). In the same time interval, the NaCl layers shorten from 2.2 mm to 1.5 mm in total (35 %  
242 shortening). This analysis also reveals how shortening was partitioned between the three layers  
243 (Fig. 5). Initially, both layers compacted at about the same rate. At 91 hours, the shortening  
244 was partitioned into the marginal NaCl layers, a development that continued to 376 hours. At  
245 137.5 hours the pore connectivity in the biotite-bearing layer broke down (see section 3.2.2  
246 below), as shown by the grey shaded area in Fig. 5. This event was followed by accelerated  
247 compaction in the biotite-bearing layer and a deceleration of compaction in the NaCl layers.  
248 From 376 hours onwards, both layers compacted at about the same rate, until the end of the  
249 experiment.

250

251 We further analysed the pore size distribution in the two sample compositions  
252 (Supplementary Fig. S5) for three compaction steps (beginning, middle and end of the  
253 compaction). In both samples, the absolute frequency of larger volume pores decreased and  
254 that of smaller pores increased with increasing compaction. In the NaCl sample, small pores  
255 (volume  $< 2.6 \times 10^5 \mu\text{m}^3$ ) doubled in frequency with increasing deformation. However, these  
256 pores contributed relatively small amounts to the total pore volume (Supplementary Fig. S5c).  
257 Similar observations were made in the NaCl-biotite sample. To better understand the effect of  
258 the central biotite-bearing layer, we analysed the pore size distributions in this layer and the  
259 marginal NaCl layers in five increasingly shortened datasets (Supplementary Fig. S6). The pore  
260 size distribution for the marginal NaCl layers showed a general increase in smaller pore sizes  
261 (volumes  $< 2.6 \times 10^5 \mu\text{m}^3$ ) and a corresponding decrease in the number of larger pores, which  
262 resembled the evolution of the pure NaCl sample (Supplementary Fig. S6a). However, the  
263 central biotite-bearing layer showed a much more marked reduction for large pores  
264 (Supplementary Fig. S6b).

265

### 266 **3.2.2. Pore Connectivity**

267 We further analysed how compaction affected pore connectivity via pore throats (as  
268 opposed to grain boundaries, which we could not resolve in our data) in the two samples. The  
269 homogeneity of the pure NaCl sample is assumed to be responsible for the preservation of a  
270 percolating pore network throughout the sample until the end of the experiment (Fig. 6). The  
271 largest connected pore cluster (volume  $> 2.7 \times 10^8 \mu\text{m}^3$ ) initially accounted for all the pore  
272 space; however, in later compaction stages  $\sim 3$  % of the porosity was accommodated by

273 smaller, isolated pores (Fig. 6 top). In contrast, the NaCl-biotite sample was characterized by a  
274 marked difference in the evolution of pore connectivity in the central NaCl-biotite layer and the  
275 marginal NaCl layers (Fig. 6 bottom). While the pore space was initially connected throughout  
276 the entire sample, with 99.8 % of the segmented porosity being accommodated by a single pore  
277 cluster, porosity started to disconnect vertically across the NaCl-biotite layer after 137.5 hours  
278 of compaction. Eventually two large pore clusters, disconnected from each other, remained  
279 present at the top and bottom of the sample, in total constituting 88 % of the total pore space  
280 (Fig. 6). A significant proportion of porosity was accommodated by smaller, isolated pores,  
281 mostly located at the interfaces with the marginal NaCl layers (not shown in Fig. 6).

### 282 **3.3 Local strains and strain rates: results from DVC analysis**

283 DVC was applied to every successive pair of compaction steps, yielding the evolving  
284 displacement fields during the entire experiment using eleven DVC datasets per sample. The  
285 DVC analysis of the pure NaCl sample showed a relatively homogeneous distribution of shear  
286 strains, with local maxima (Fig. 7, Supplementary Gif1). These zones correspond to zones where  
287 the volumetric strain is negative, indicating compaction (white circles in Fig. 7).

288 In comparison, the DVC analysis of the NaCl-biotite sample showed a much more  
289 heterogeneous shear strain distribution at the beginning and again at the end of the  
290 experiment, with a concentration of shear strains in the NaCl-biotite layer (Fig. 8,  
291 Supplementary Gif2). The analyses of volumetric strains in this sample showed a concentration  
292 of compaction in the centre of the sample (white circles in Fig. 8), with the highest strains being  
293 accumulated in the early and late stages of the experiment.

294 Calculating the local integrated strain rates from DVC analyses enabled contrasting the  
295 bulk compaction rate of each sample with locally resolved strain rates on the grain scale (Fig. 9).  
296 While in both samples the bulk compaction rates decreased by two orders of magnitude during  
297 the duration of the experiment ( $10^{-6}$  to  $10^{-8}$   $s^{-1}$ , Fig.2), locally (i.e. on the grain scale) both  
298 samples showed significant deviations in strain rates (Fig. 2). In the pure NaCl sample, the local  
299 shear strain rates decreased from  $10^{-6} - 10^{-7}$  to  $10^{-8} - 10^{-9}$   $s^{-1}$ , whereas volumetric strain rates  
300 decreased from  $-10^{-6}$  to  $-10^{-8}$   $s^{-1}$  in the most compacted areas. However, these values were  
301 evenly distributed within the sample (Fig. 9). In contrast, the shear strain rates reached  
302 maximum values of  $10^{-7}$   $s^{-1}$  in the presence of biotite, while the highest volumetric compaction  
303 rates were  $-6 \times 10^{-8}$   $s^{-1}$ . The high shear- and lower volumetric strain rates occur in the central  
304 NaCl-biotite layers (Fig. 9) and are an order of magnitude higher than in the rest of the sample.

### 305 **3.4 Microstructural evidence for PSC**

306 SEM images of the recovered samples were acquired in order to verify the  
307 microstructural changes and to collect evidence for PSC, if present, on the grain scale (Fig. 10).  
308 Indented contacts would provide evidence for PSC consistent with that proposed by Passchier  
309 and Trouw (2005) (page 31, box 3.2). In the pure NaCl sample, grains that have lost their  
310 original cubic habits are clearly visible (Fig. 10a, b). In some areas, it is possible to recognize  
311 triple junctions (Fig. 10a) and suture zones between grain interfaces, where the two grain  
312 contacts are highly indented (Fig. 10b). In the presence of phyllosilicates, indentations are  
313 obvious and NaCl grains can be seen that have dissolved against (less soluble) biotite grains,  
314 and NaCl grains that have lost their cubic habit and have become more rounded are also

315 evident (Fig. 10c, d). In the pure NaCl portions of this sample, indentations between NaCl grains  
316 can still be observed, but the grains have retained more of their original habit (Fig. 3).

## 317 **4. DISCUSSION**

### 318 **4.1 Bulk and local deformation evolution**

319 Our experiments enable a direct comparison of bulk compaction behaviour with local  
320 grain-scale responses and thus allow novel insights into the effects of sample composition on  
321 the deformation processes. The bulk compaction curves of the two investigated sample  
322 configurations (Fig. 2a) show a strong non-linear decrease in the compaction rate over time,  
323 which is in agreement with findings from previous studies and support our conclusion that NaCl  
324 deforms by PSC (Hickman and Evans, 1995, 1991; Renard et al., 2004; Schutjens and Spiers,  
325 1999; Spiers et al., 1990). However, the duration of our experiments considerably exceeded  
326 that of many published studies (Renard et al., 2004; Rutter and Wanten, 2000; Spiers et al.,  
327 1990;), which allows a more detailed assessment of the evolution of compaction behaviour of  
328 halite samples. Earlier, shorter studies by Renard et al. (2004) and Spiers et al. (1990) showed a  
329 very similar compaction behaviour despite slightly different experimental setups. Renard et al.  
330 (2004) used a smaller grain size of sieved NaCl (100-150  $\mu\text{m}$ ), and smaller loads (0.1 to 0.6 MPa)  
331 and conducted their experiment at room temperature for seven days. The compaction rate  
332 decreased over time, showing an initial steep gradient, as in our data, and reaching 18 % of  
333 vertical shortening after three days. They concluded that the presence of clays supports grain  
334 contact healing, reducing porosity and favouring pressure-solution creep. Spiers et al. (1990)  
335 performed tests on brine-saturated NaCl powder (grain size 100-275  $\mu\text{m}$ ) at temperatures of  
336 20-90°C and applied stresses of 0.5-2.2 MPa, testing theoretically-derived constitutive



337 equations. Their grain sizes and time intervals are similar to ours, and their results showed  
338 similar orders of bulk strain rates. The data presented here explore the time evolution beyond  
339 the initial steep compaction rate shown in these studies and provide a visual assessment of the  
340 micro-scale processes, feeding into a better understanding of the role of phyllosilicates.

341         The striking observation from our own experiments is that both samples follow  
342 essentially the same bulk compaction path, with a very rapid initial compaction characterized  
343 by variable rates (Fig. 2 a, b), replaced by what appears to be steady state compaction after  
344 about 400 hours. We interpret mechanical grain rearrangements and accelerated dissolution  
345 rates at initially relatively small and, therefore, highly stressed grain contact areas to be  
346 responsible for the high compaction rates during the early stages of the experiments. The  
347 decrease in the compaction rate up to about 400 hours might broadly reflect an increase in  
348 grain contact area and the associated decrease in local normal stresses as drivers for  
349 dissolution.

350         From about 400 hours until the end of the experiments at 2455 hours, both experiments  
351 compacted by PSC at virtually the same constant rates (Fig. 2b), which raises questions about  
352 the actual effect of biotite upon PSC in the NaCl-biotite sample. In our interpretation, we  
353 consider it of importance that, while the local shear strain rates reached up to  $3 \times 10^{-8} \text{ s}^{-1}$  in the  
354 pure NaCl sample, these maxima tended to be transient in terms of their location and moved  
355 throughout the sample (cf. Fig. 9a). We interpret this as the capture of dynamic  
356 rearrangements of stresses in the compacting sample (see below). The NaCl-biotite sample  
357 showed similar magnitudes of local strain rates, but in that case, these were clearly associated  
358 with the loci of biotite flakes and remained so over the entire duration of the experiment (Fig.

359 8, 9). We further observe that the presence of biotite was clearly related to the reduction of  
360 porosity (Fig. 4 b-d), which, in the absence of strain localization in the central NaCl-biotite layer  
361 (Fig. 5), cannot be ascribed to pore collapse there and rather points to pores having been filled.

362

363         On the basis of these observations, we interpret PSC in the NaCl and NaCl-biotite layers,  
364 to have operated under different conditions in the two layers. We envisage the overall load in  
365 pure granular NaCl samples, at least initially, to have been distributed over “force chains”. The  
366 concept of force chains in compacting granular materials considers the overall load to be  
367 distributed heterogeneously among the grains, with a minority of grains that carry above-  
368 average loads forming a strong load-bearing framework, while the majority of grains constitute  
369 a weak granular aggregate (e.g. Peters et al., 2005). In our conceptual model, a force chain will  
370 localize pressure solution in a granular NaCl aggregate along an axis that is broadly aligned with  
371 the bulk shortening direction and over an initially small grain contact area. The idea of *dynamic*  
372 *force chains* entails that the lifetime of a particular force chain is limited by the dynamic  
373 redistribution of loads within the granular aggregate as locally increased normal stresses lead to  
374 enhanced PSC and accelerated shortening, and a relative increase of the grain surface area  
375 along the force chain. When loads are redistributed, the load-bearing framework changes its  
376 geometry. Our DVC analysis indicates that the strain within the pure NaCl sample varies in  
377 space and time; we interpret this to indicate a rearrangement of stresses and the emergence of  
378 new dynamic force chains in the pure NaCl layers.

379         While, in principal, the conceptual model described above may also apply to the NaCl-  
380 biotite layer, our DVC analysis indicates that compaction there was tied to the biotite grains and

381 we interpret PSC to have been accelerated by the higher chemical potential associated with  
382 phase boundaries (Aharonov and Katsman, 2009; Hickman and Evans, 1995). Factors such as  
383 particle shape, particle size, and contact area may also have played a significant role in  
384 controlling the evolution of PSC. Meyer et al. (2006) and Van den Ende et al.(2018)  
385 demonstrated how particle shapes and the shape of the contact between the particles  
386 influence compaction rates in pressure-solution. Pluymakers and Spiers (2015) emphasized the  
387 significance of the nature of the contact surfaces where irregularities lead to faster dissolution.  
388 The initial geometric arrangement of the grain contacts between a cube and a plate-like mineral  
389 (i.e. salt vs biotite) may create ‘asperities’, with lower contact areas, which could have assisted  
390 the driving force of the mechanism. From 400 hours onward, the process might have slowed  
391 down because reduced porosity was met by reduced asperities/irregularities in the grains,  
392 which became progressively smoother as compaction progressed (lower contact stresses). We  
393 envisage that these mechanisms contributed to pressure solution. Whichever the reason, the  
394 local strain rate data from our DVC analysis suggest that this enhanced PSC drove the initial  
395 compaction in the NaCl-biotite layer (Fig. 9). However, with increasing shortening, the contact  
396 areas in the NaCl layer increased, which lowered the stresses at contact points and, as a  
397 consequence reduced the driving force for PSC. DVC reveals that both the local volumetric and  
398 the shear strain rates decreased by almost an order of magnitude in the NaCl-biotite layer  
399 between 150 and 400 hours of compaction (Fig. 9, central column), which we consider to be  
400 supporting evidence for this interpretation.

401           Compaction of the central NaCl-biotite layer was accompanied by a significant reduction  
402 of the porosity, to such a degree that pore connectivity broke down across the central layer

403 early in the experiment (Fig. 3, 4 and 6). However, at the same time, this layer did not compact  
404 significantly more than the surrounding NaCl layers (Fig. 5). It is generally assumed that the  
405 transport distances during pressure solution of NaCl in a stagnant, saturated brine are on the  
406 order of the grain size and material is re-precipitated in the nearby pore space (e.g. Gratier et  
407 al., 2013; Gundersen et al., 2002; Weyl, 1959). For our experiments this would mean that the  
408 porosity in the NaCl and NaCl-biotite layers should have decreased in proportion with the  
409 compaction. Given that this was clearly not the case, porosity reduction in the NaCl-biotite layer  
410 cannot have been accomplished by pore collapse during compaction. We speculate that the  
411 disproportional decrease of porosity in the NaCl-biotite layer was caused by additional salt  
412 being deposited there and, invoke Merino et al.'s model for a texture-pressure solution  
413 coupling to explain this (Dewers and Ortoleva, 1988; Merino et al., 1983; Ortoleva et al., 1987).  
414 Merino suggests that, in a positive feedback loop, dissolved material should diffuse towards  
415 areas with a relatively lower porosity and, therefore, larger grain contact area and  
416 correspondingly lower stresses. In our experiment, this would mean that material was  
417 transported from the pure NaCl layers to the central NaCl-biotite layer. In the former, the  
418 removal of dissolved material leaves less material to carry the load, which increases the driving  
419 force for PSC. At the same time, loads are distributed over an increasingly larger area at the  
420 deposition sites in the NaCl-biotite layer, which should slow down PSC there. We interpret our  
421 quantitative observations to provide evidence that dissolved salt has indeed been transferred  
422 from the marginal NaCl into the central NaCl-biotite domain. Once connectivity into the NaCl-  
423 biotite was lost, the interface between the two domains would have become the locus for  
424 enhanced deposition (Fig. 3).

## 425 **4.2 Implications for fluid flow and permeability in rocks deforming by PSC**

426 Our experiments provide new insights into the effects of PSC on the spatio-temporal  
427 evolution of porosity and pore connectivity, which influence transport properties, and  
428 consequently fluid flow. These effects have been intensively studied, particularly for the case of  
429 stylolites. Stylolites commonly develop in carbonates, silicate rocks, sandstones and mudstones  
430 (Benedicto and Schultz, 2010; Gratier et al., 2013; Heap et al., 2014; Park and Schot, 1968).  
431 They can induce up to 50 % of dissolution in the host rock with important implication for solute  
432 transport and fluid flow (Aharonov and Katsman, 2009). However, it remains unclear whether  
433 stylolites act as barriers to fluid flow (Alsharhan and Sadd, 2010) or become fluid conduits  
434 (Heap et al., 2014;). Our experiments, which were conducted under the reported, specific  
435 boundary conditions, show that the disconnection of the pore space with increasing  
436 deformation leads to a very efficient hydraulic compartmentalization of the sample. The  
437 porosity evolution in the central layer would suppress any potential fluid flow across the layer  
438 and constrain fluid movements to the NaCl layers, at least at the scale and resolution of our  
439 data. At the same time, it would allow fluid that is trapped inside the NaCl-biotite layer to  
440 equilibrate chemically with its local host, whereas fluid in the percolating NaCl layers would  
441 form part of an open chemical system. Our results support the interpretation by Heap et al.  
442 (2014) that stylolites may compartmentalize fluid flow, allowing movement in the marginal  
443 layers and in the directions perpendicular to the shortening direction.

444

445 Our findings feed into an improved understanding of fluid transport properties in  
446 hydrocarbon reservoirs where PSC is active (Ghanbarzadeh et al., 2015; Torabi et al., 2015).

447 Alsharhan and Sadd (2010) and Heap et al. (2014) show that stylolites are capable of reducing  
448 permeability when the rock is enriched in minerals such as phyllosilicates. The effect of biotite  
449 on the permeability of the halite rocks remains unclear and will be addressed using a modelling  
450 approach in a follow-up study.

## 451 **5. CONCLUSIONS**

452 We have analysed the first 4D microtomographic dataset that documents pressure  
453 solution creep in NaCl-biotite aggregates over several months. Our results indicate that  
454 phyllosilicates contribute to reduce bulk porosity and induce a significant decrease in pore  
455 connectivity, causing a hydraulic compartmentalization of the sample. The measured local  
456 strain rates indicate that phyllosilicates enhance the pressure-solution process by increasing the  
457 local strain rates. These results highlight the key role of phyllosilicates in affecting the rock  
458 microstructure under pressure-solution creep and provide new insights into the spatio-  
459 temporal evolution of transport properties.

## 460 **ACKNOWLEDGEMENTS**

461 The authors would like to thank Dr. Nicola Cayzer for help at the SEM and Robert Brown and  
462 Alex Hart for manufacturing the experimental cells and straining frames. All three are from the  
463 School of Geosciences, University of Edinburgh. We furthermore thank Dr. Anne Pluymakers  
464 and an anonymous reviewer for extremely encouraging and constructive reviews. The work was  
465 supported by the PhD studentship funding from the School of Geosciences, University of  
466 Edinburgh.

## 467 **REFERENCES**

468 Aharonov, E., Katsman, R., 2009. Interaction between pressure solution and clays in stylolite  
469 development: Insights from modeling. *Am. J. Sci.* 309, 607–632.  
470 <https://doi.org/10.2475/07.2009.04>

471 Alsharhan, A.S., Sadd, A.L., 2010. Stylolites in Lower Cretaceous Carbonate Reservoirs, U.A.E.  
472 *Soc. Sediment. Geol.* <https://doi.org/10.2110/pec.00.69.0185>

473 Andò, E., Bésuelle, P., Hall, S.A., Viggiani, G., Desrues, J., 2012. Experimental micromechanics:  
474 grain-scale observation of sand deformation. *Géotechnique Lett.* 2, 107–112.  
475 <https://doi.org/10.1680/geolett.12.00027>

476 Angevine, C.L., Turcotte, D.L., 1983. Porosity reduction by pressure solution: a theoretical  
477 model for quartz arenites. *Geol Soc Amer Bull* 94, 1129–1134.  
478 [https://doi.org/10.1130/0016-7606\(1983\)94<1129](https://doi.org/10.1130/0016-7606(1983)94<1129)

479 Arns, C.H., Knackstedt, M.A., Pinczewski, W. V., Garboczi, E.J., 2002. Computation of linear  
480 elastic properties from microtomographic images: Methodology and agreement between  
481 theory and experiment. *Geophysics* 67, 1396. <https://doi.org/10.1190/1.1512785>

482 Atkinson, M., Bell, A., Curtis, A., Entwistle, E., Filgueira, R., Main, I., Meles, G., Minitier, M., Zhao,  
483 Y., 2015. The Terracorrelator : a shared memory HPC facility for real-time seismological  
484 cross-correlation analyses. *Geophys. Res. Abstr. Eur. Geosci. Union Gen. Assem.* 17.

485 Benedicto, A., Schultz, R.A., 2010. Stylolites in limestone: Magnitude of contractional strain  
486 accommodated and scaling relationships. *J. Struct. Geol.* 32, 1250–1256.  
487 <https://doi.org/10.1016/j.jsg.2009.04.020>

488 Bos, B., Spiers, C.J., 2002. Frictional-viscous flow of phyllosilicate-bearing fault rock :  
489 Microphysical model and implications for crustal strength profiles. *J. Geophys. Res.* 107,

490 2028.

491 Cnudde, V., Boone, M.N., 2013. High-resolution X-ray computed tomography in geosciences: A  
492 review of the current technology and applications. *Earth-Science Rev.* 123, 1–17.  
493 <https://doi.org/10.1016/j.earscirev.2013.04.003>

494 Croizé, D., Bjørlykke, K., Jahren, J., Renard, F., 2010. Experimental mechanical and chemical  
495 compaction of carbonate sand. *J. Geophys. Res. Solid Earth* 115, 1–17.  
496 <https://doi.org/10.1029/2010JB007697>

497 Dewers, T., Ortoleva, P., 1988. The role of geochemical self-organization in the migration and  
498 trapping of hydrocarbons. *Appl. Geochemistry* 3, 287–316. [https://doi.org/10.1016/0883-](https://doi.org/10.1016/0883-2927(88)90108-4)  
499 [2927\(88\)90108-4](https://doi.org/10.1016/0883-2927(88)90108-4)

500 Dierick, M., Masschaele, B., Hoorebeke, L. Van, 2004. Octopus, a fast and user-friendly  
501 tomographic reconstruction package developed in LabView®. *Meas. Sci. Technol.* 15,  
502 1366–1370. <https://doi.org/10.1088/0957-0233/15/7/020>

503 Fusseis, F., Schrank, C., Liu, J., Karrech, A., Llana-F??nez, S., Xiao, X., Regenauer-Lieb, K., 2012.  
504 Pore formation during dehydration of a polycrystalline gypsum sample observed and  
505 quantified in a time-series synchrotron X-ray micro-tomography experiment. *Solid Earth* 3,  
506 71–86. <https://doi.org/10.5194/se-3-71-2012>

507 Ghanbarzadeh, S., Hesse, M.A., Prodanović, M., Gardner, J.E., 2015. Deformation-assisted fluid  
508 percolation in rock salt. *Science (80-. )*. 350, 1069–1072.  
509 <https://doi.org/10.1126/science.aac8747>

510 Gratier, J.P., 2003. Modeling fluid transfer along California faults when integrating pressure  
511 solution crack sealing and compaction processes. *J. Geophys. Res.* 108, 1–25.



512 <https://doi.org/10.1029/2001JB000380>

513 Gratier, J.P., 1993. Experimental pressure solution of halite by an indenter technique. *Geophys.*  
514 *Res. Lett.* 20, 1647–1650.

515 Gratier, J.P., Dysthe, D.K., Renard, F., 2013. The role of pressure solution creep in the ductility of  
516 the Earth ' s upper crust, *Advances in Geophysics*. [https://doi.org/10.1016/B978-0-12-](https://doi.org/10.1016/B978-0-12-380940-7.00002-0)  
517 [380940-7.00002-0](https://doi.org/10.1016/B978-0-12-380940-7.00002-0)

518 Gratier, J.P., Muquet, L., Hassani, R., Renard, F., 2005. Experimental microstylolites in quartz  
519 and modeled application to natural stylolitic structures. *J. Struct. Geol.* 1–24.

520 Gundersen, E., Renard, F., Dysthe, D.K., Bjørlykke, K., Jamtveit, B., 2002. Coupling between  
521 pressure solution creep and diffusive mass transport in porous rocks. *J. Geophys. Res. Solid*  
522 *Earth* 107, ECV 19-1-ECV 19-19. <https://doi.org/10.1029/2001JB000287>

523 Heap, M.J., Baud, P., Reuschle, T., Meredith, P.G., 2014. Stylolites in limestones: Barriers to fluid  
524 flow? *Geology* 42, 51–54. [https://doi.org/doi: 10.1130/G34900.1](https://doi.org/doi:10.1130/G34900.1)

525 Hickman, S.H., Evans, B., 1995. Kinetics of pressure solution at halite-silica interfaces and  
526 intergranular clay films. *J. Geophys. Res. Earth* 100, 13113–13132.  
527 <https://doi.org/10.1029/95JB00911>

528 Hickman, S.H., Evans, B., 1991. Experimental pressure solution in halite : the effect boundary  
529 structure of grain / interphase. *J. Geol. Soc. London.* 148, 549–560.  
530 <https://doi.org/10.1144/gsjgs.148.3.0549>

531 Lehner, F., Leroy, Y., 2004. Sandstone Compaction by Intergranular Pressure Solution. Guéguen,  
532 Y., Boutéca, M. (Eds.), *Mech. Fluid-Saturated Rocks. Int. Geophys. Ser. Vol. 89*, pp. 115–168  
533 2004. 1–54.

534 Macente, A., Fousseis, F., Menegon, L., Xianghui, X., John, T., 2017. The strain-dependent spatial  
535 evolution of garnet in a high-P ductile shear zone from the Western Gneiss Region  
536 (Norway): a synchrotron X-ray microtomography study. *J. Metamorph. Geol.* 35, 565–583.  
537 <https://doi.org/10.1111/jmg.12245>

538 Merino, E., Ortoleva, P., Strickholm, P., 1983. Generation of evenly-spaced pressure-solution  
539 seams during (late) diagenesis: A kinetic theory. *Contrib. to Mineral. Petrol.* 82, 360–370.  
540 <https://doi.org/10.1007/BF00399713>

541 Meyer, E.E., Greene, G.W., Alcantar, N.A., Israelachvili, J.N., Boles, J.R., 2006. Experimental  
542 investigation of the dissolution of quartz by a muscovite mica surface: Implications for  
543 pressure solution. *J. Geophys. Res. Solid Earth* 111, 1–4.  
544 <https://doi.org/10.1029/2005JB004010>

545 Ortoleva, P., Merino, E., Moore, C., Chadam, J., 1987. Geochemical self-organization I: reaction-  
546 transport feedbacks and modeling approach. *Am. J. Sci.*  
547 <https://doi.org/10.2475/ajs.287.10.979>

548 Park, W.C., Schot, E.H., 1968. Stylolites: their nature and origin. *J. Sediment. Res.* 38, 175–191.  
549 <https://doi.org/10.1306/74D71910-2B21-11D7-8648000102C1865D>

550 Passchier, C.W., Trouw, R.A.J., 2005. *Microtectonics*.

551 Peters, J.F., Muthuswamy, M., Wibowo, J., Tordesillas, A., 2005. Characterization of force chains  
552 in granular material. *Phys. Rev. E - Stat. Nonlinear, Soft Matter Phys.* 72, 1–8.  
553 <https://doi.org/10.1103/PhysRevE.72.041307>

554 Pluymakers, A.M.H., Spiers, C.J., 2015. Compaction creep of simulated anhydrite fault gouge by  
555 pressure solution: Theory v. experiments and implications for fault sealing. *Geol. Soc. Spec.*

556 Publ. 409, 107–124. <https://doi.org/10.1144/SP409.6>

557 Renard, F., Bernard, D., Thibault, X., Boller, E., 2004. Synchrotron 3D microtomography of halite  
558 aggregates during experimental pressure solution creep and evolution of the permeability.  
559 Geophys. Res. Lett. 31, 1–4. <https://doi.org/10.1029/2004GL019605>

560 Renard, F., Dysthe, D., Feder, J., Bjorlykke, K., Jamtveit, B., 2001. Enhanced pressure solution  
561 creep rates induced by clay particles: Experimental evidence in salt aggregates. Geophys.  
562 Res. Lett. 28, 1295–1298. <https://doi.org/10.1029/2000GL012394>

563 Renard, F., Ortoleva, P., Gratier, J.P., 1997. Pressure solution in sandstones: influence of clays  
564 and dependence on temperature and stress. Tectonophysics 280, 257–266.  
565 [https://doi.org/10.1016/S0040-1951\(97\)00039-5](https://doi.org/10.1016/S0040-1951(97)00039-5)

566 Rutter, E.H., 1983. Pressure solution in nature, theory and experiment. J. Geol. Soc. London.  
567 140, 725–740. <https://doi.org/10.1144/gsjgs.140.5.0725>

568 Rutter, E.H., Wanten, P.H., 2000. Experimental Study of the Compaction of Phyllosilicate-  
569 Bearing Sand at Elevated Temperature and with Controlled Pore Water Pressure. J.  
570 Sediment. Res. 70, 107–116. [https://doi.org/10.1306/2DC40902-0E47-11D7-  
571 8643000102C1865D](https://doi.org/10.1306/2DC40902-0E47-11D7-8643000102C1865D)

572 Schindelin, J., Arganda-Carreras, I., Frise, E., Kaynig, V., Longair, M., Pietzsch, T., Preibisch, S.,  
573 Rueden, C., Saalfeld, S., Schmid, B., Tinevez, J.-Y., White, D.J., Hartenstein, V., Eliceiri, K.,  
574 Tomancak, P., Cardona, A., 2012. Fiji: an open-source platform for biological-image  
575 analysis. Nat. Methods 9, 676–682. <https://doi.org/10.1038/nmeth.2019>

576 Schutjens, P.M.T.M., Spiers, C.J., 1999. Intergranular pressure solution in NaCl: Grain-to-grain  
577 contact experiments under the optical microscope. Oil Gas Sci. Technol. 54, 729–750.

578 <https://doi.org/10.2516/ogst:1999062>

579 Spiers, C.J., Schutjens, P.M.T.M., Brzesowsky, R.H., Peach, C.J., Liezenberg, J.L., Zwart, H.J.,  
580 1990. Experimental determination of constitutive parameters governing creep of rocksalt  
581 by pressure solution. *Geol. Soc. London, Spec. Publ.* 54, 215–227.  
582 <https://doi.org/10.1144/GSL.SP.1990.054.01.21>

583 Sprunt, E.S., Nur, A., 1977. Destruction of porosity through pressure solution. *Geophysics* 42,  
584 726–741.

585 Sprunt, E.S., Nur, A., 1976. Reduction of porosity by pressure solution: Experimental  
586 verification. *Geology* 4, 463–466.

587 Torabi, A., R.H., G., Fossen, H., Pingrose, P., Skurtveit, E., Ando', E., 2015. Strain localization in  
588 sandstone and its implications for CO2 storage. *First Break* 33, 81–92.

589 Tudisco, E., Andò, E., Cailletaud, R., Hall, S.A., 2017. TomoWarp2: A local digital volume  
590 correlation code. *SoftwareX* 6, 267–270. <https://doi.org/10.1016/j.softx.2017.10.002>

591 Van den Ende, M.P.A., Marketos, G., Niemeijer, A.R., Spiers, C.J., 2018. Investigating  
592 Compaction by Intergranular Pressure Solution Using the Discrete Element Method. *J.*  
593 *Geophys. Res. Solid Earth*. <https://doi.org/10.1002/2017JB014440>

594 Weyl, P.K., 1959. Pressure solution and the force of crystallization: a phenomenological theory.  
595 *J. Geophys. Res.* 64, 2001–2025. <https://doi.org/10.1029/JZ064i011p02001>

## 596 **FIGURE CAPTIONS**

597 **Figure 1** a) Horizontal XY  $\mu$ CT slice and b) vertical XZ  $\mu$ CT slice of the NaCl-biotite sample,  
598 showing the different attenuation values of the materials: biotite in bright colour, NaCl grains in  
599 light grey and (brine-filled) pores in dark grey.

600 **Figure 2** a) Compaction curves for the two samples (top). Roman numbers indicated the  
601 number of the 12  $\mu$ CT dataset acquired: the reference scan is not numbered (see section 3.2).

602 b) Evolution of bulk strain rates with increasing deformation for the two samples, in log-log  
603 scale.

604 **Figure 3** Vertical  $\mu$ CT slices of four different shortened datasets, for pure NaCl (left column) and  
605 NaCl-biotite samples (right column), respectively. Roman numbering refers to Figure 2a. White  
606 arrows indicate areas of reduced porosity, where NaCl grains indent more, losing their cubic  
607 habit, and/or precipitation sites.

608 **Figure 4** a) Evolution of the pore volume (in  $\mu\text{m}^3$ ) in the two sample compositions for increasing  
609 compaction time (hours). The percentages inside the bars indicate the porosity, calculated  
610 through the *Volume Fraction* operator from the  $400^3$  voxels subvolumes (see section 2.2.4).  
611 Initial porosity fraction ( $\phi_0$ ), calculated from the undeformed  $400^3$  voxels subvolumes, is given  
612 in the legend for the two samples. Errors bars obtained through erosion and dilation of original  
613 segmented pore space. b, c, d) Temporal evolution (in hours, 'hs') of porosity slice by slice  
614 ("Porosity 2D") as a function of the vertical Z axis for the two samples.

615 **Figure 5** Relative shortening of the biotite-bearing and NaCl-bearing layers. The grey shaded  
616 area indicates the time interval over which pore connectivity breaks down within the NaCl-  
617 biotite layer (see section 3.2.2).

618 **Figure 6** Interconnectivity of the pore space as a function of deformation for the two samples.  
619 Different colours indicate disconnected pore clusters.

620 **Figure 7** DVC results for the NaCl sample, for increasing compaction time (indicated in hours,  
621 'hs') and vertical shortening (in percentage). Images are obtained as vertical slices through the

622 middle of the sample. For a better comparison, maximum shear strain (*Shear Strain*) and  
623 volumetric strain (*Volum. Strain*) results are reported together with the pair of *x-ray*  $\mu$ CT images  
624 used for the correlation for each interval time. Black areas identify locations where the  
625 correlation failed. Higher values of maximum shear strain are represented in the images by  
626 warmer colours, while negative values of volumetric strain (indicating compaction) are  
627 represented by blue colours (white circles). Note the relatively homogeneous distribution of  
628 shear strains, with local highs.

629 **Figure 8** DVC results for the NaCl-biotite sample, for increasing compaction time (indicated in  
630 hours, 'hs') and vertical shortening (in percentage). Images are obtained as vertical slices  
631 through the middle of the sample. For a better comparison, maximum shear strain (*Shear*  
632 *Strain*) and volumetric strain (*Volum. Strain*) results are reported together with the pair of *x-ray*  
633  $\mu$ CT images used for the correlation for each interval time. Black areas identify locations where  
634 the correlation failed. Higher values of maximum shear strain are represented in the images by  
635 warmer colours, while negative values of volumetric strain (indicating compaction) are  
636 represented by blue colours (white circles). Note the extreme intense values in areas where the  
637 biotite flakes are located (high shear strains, negative volumetric strains).

638 **Figure 9** The images show the distributions of local strain rates (in  $s^{-1}$ ), calculated from DVC  
639 results, for both samples: a) maximum shear strain rates, b) volumetric strain rates. To obtain  
640 the strain rates, the strain values, obtained from the DVC results, are divided by the time  
641 interval between each pair of correlations. Black areas identify locations where the correlation  
642 failed.

643 **Figure 10** SEM images of recovered samples: a) triple junction (highlighted by white arrows)  
644 between grains in the pure NaCl sample; b) close up from the red square in a, note the suture  
645 zone (white arrows) between NaCl grains; c, d) NaCl grains indenting biotite flakes (Bt) in the  
646 NaCl-biotite sample.

647

Figure1  
[Click here to download high resolution image](#)

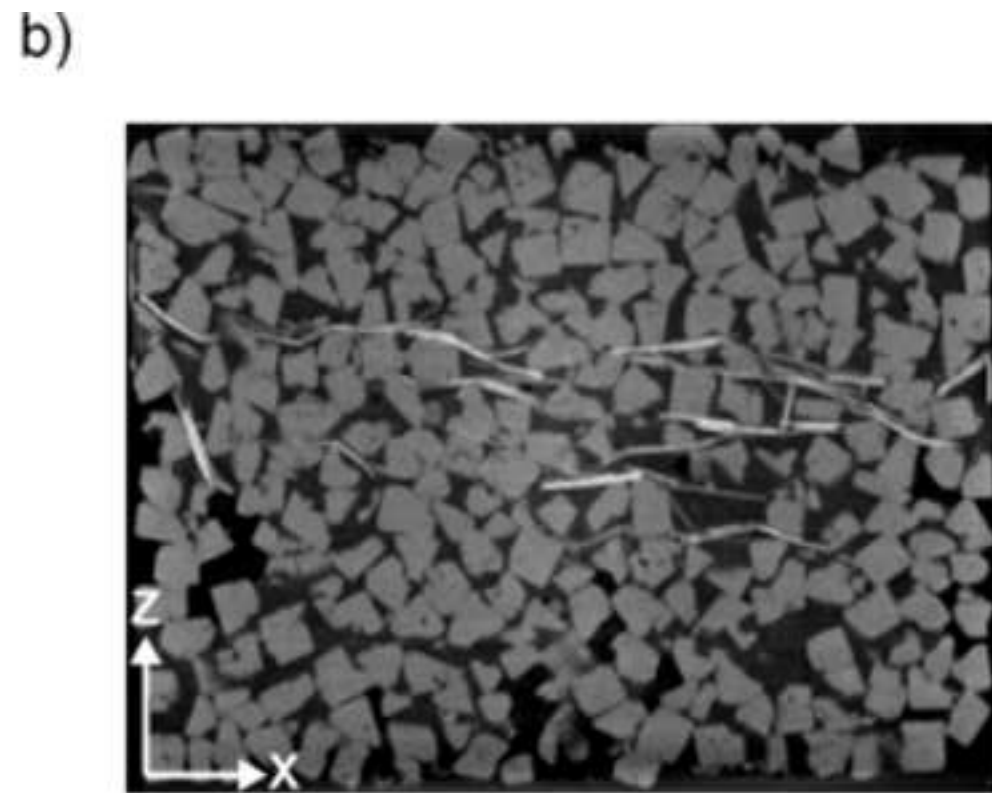
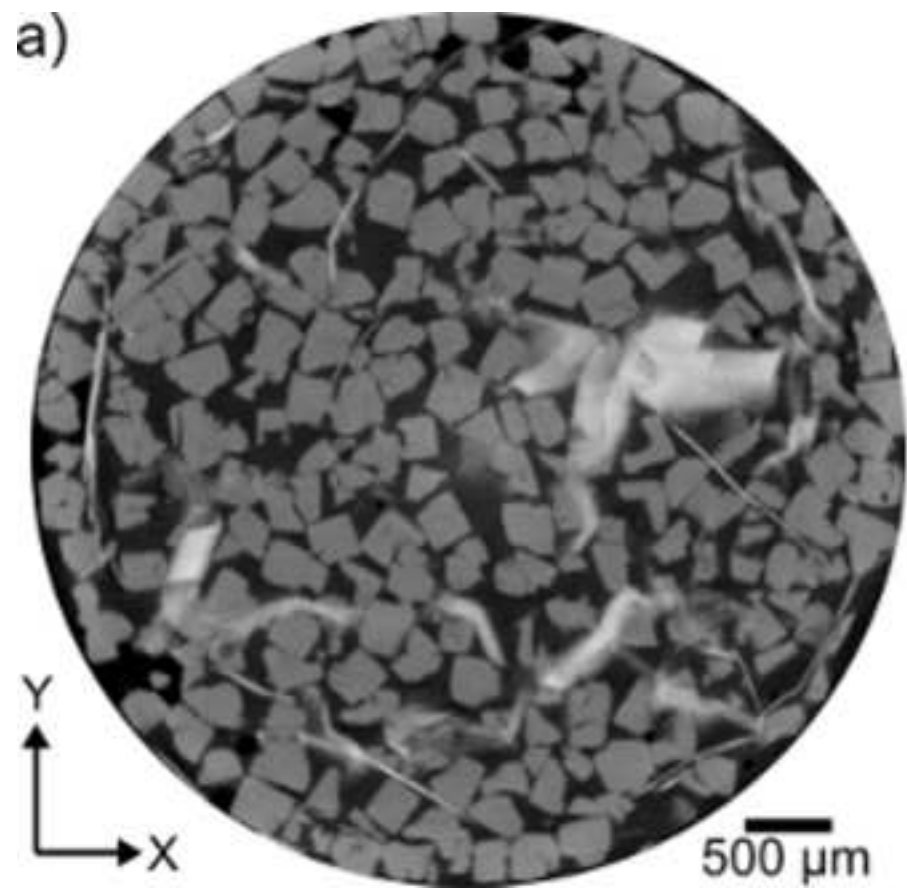




Figure 2  
[Click here to download Figure: Figure2.pdf](#)

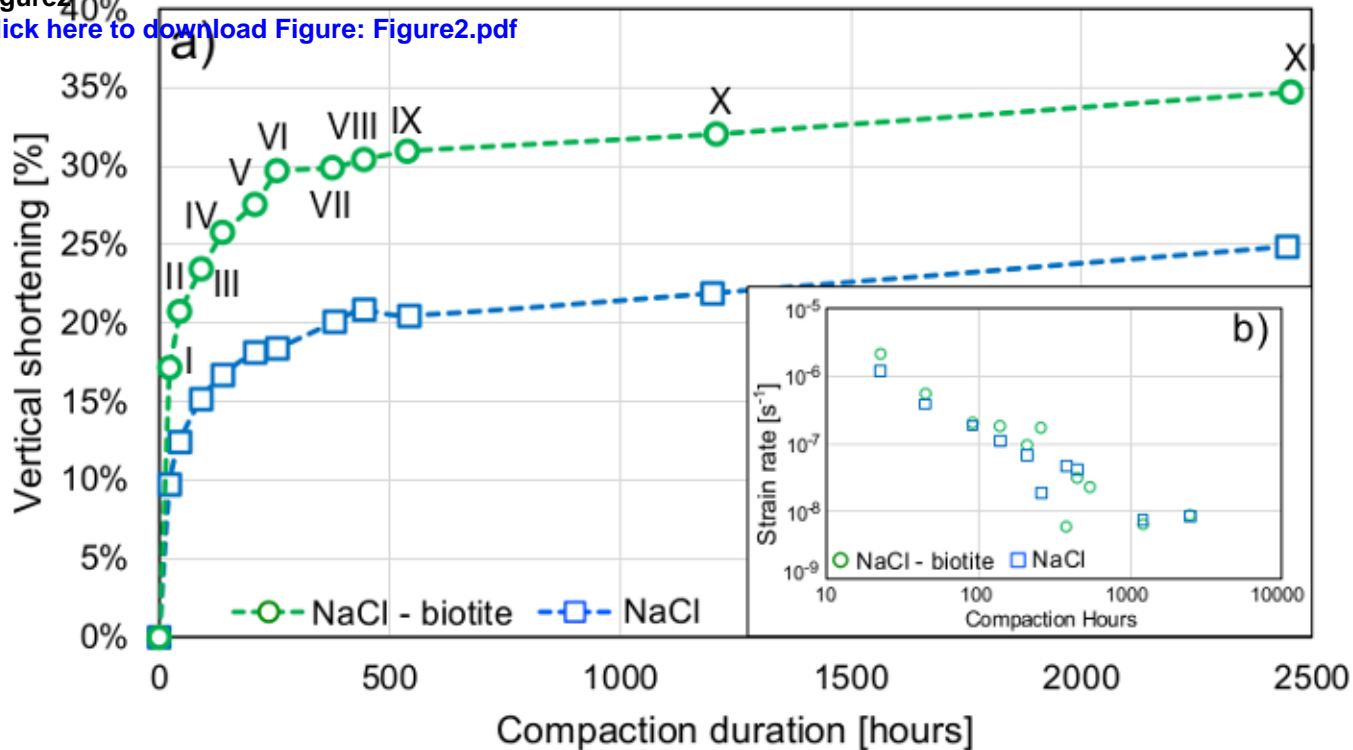


Figure3  
[Click here to download high resolution image](#)

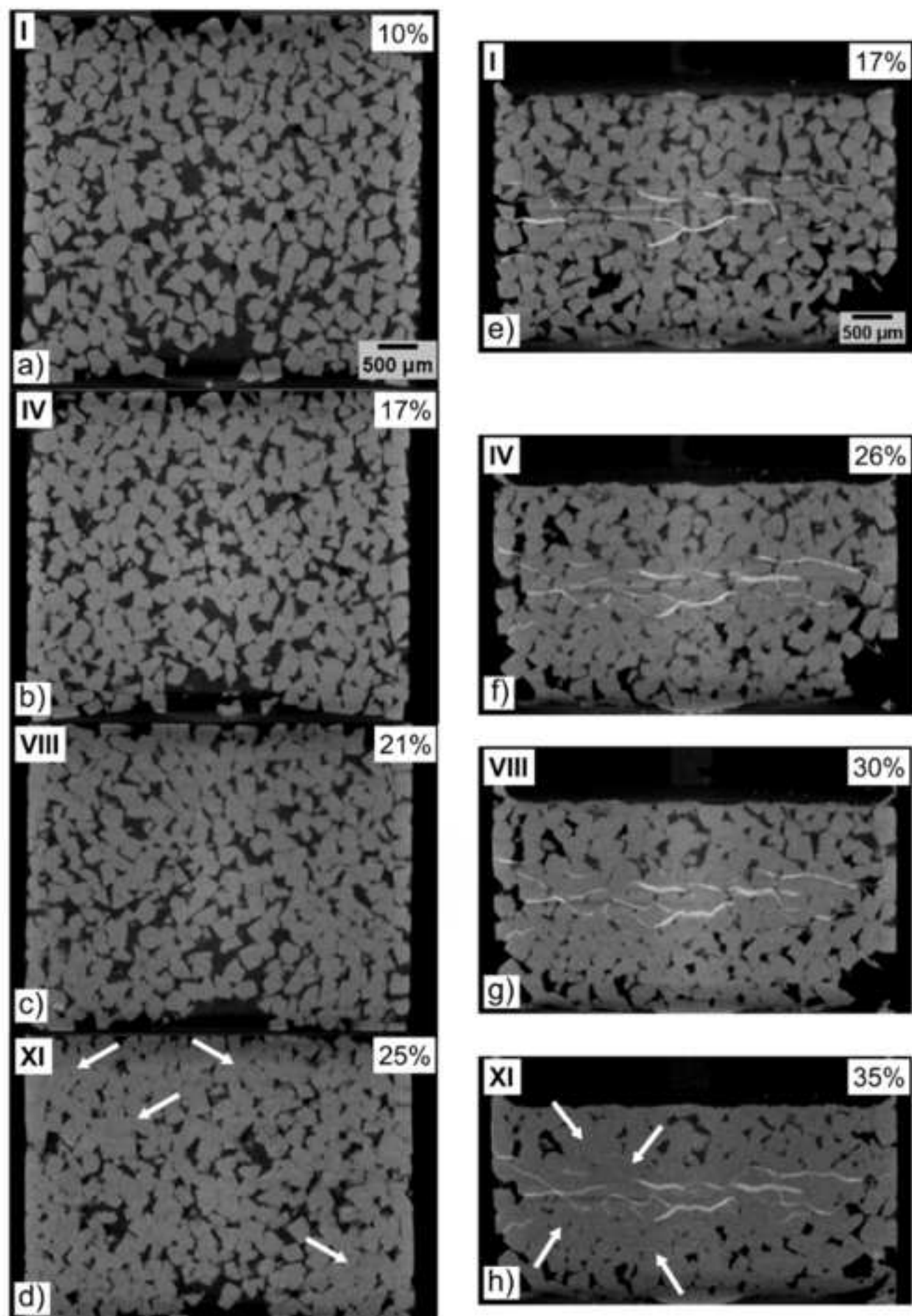
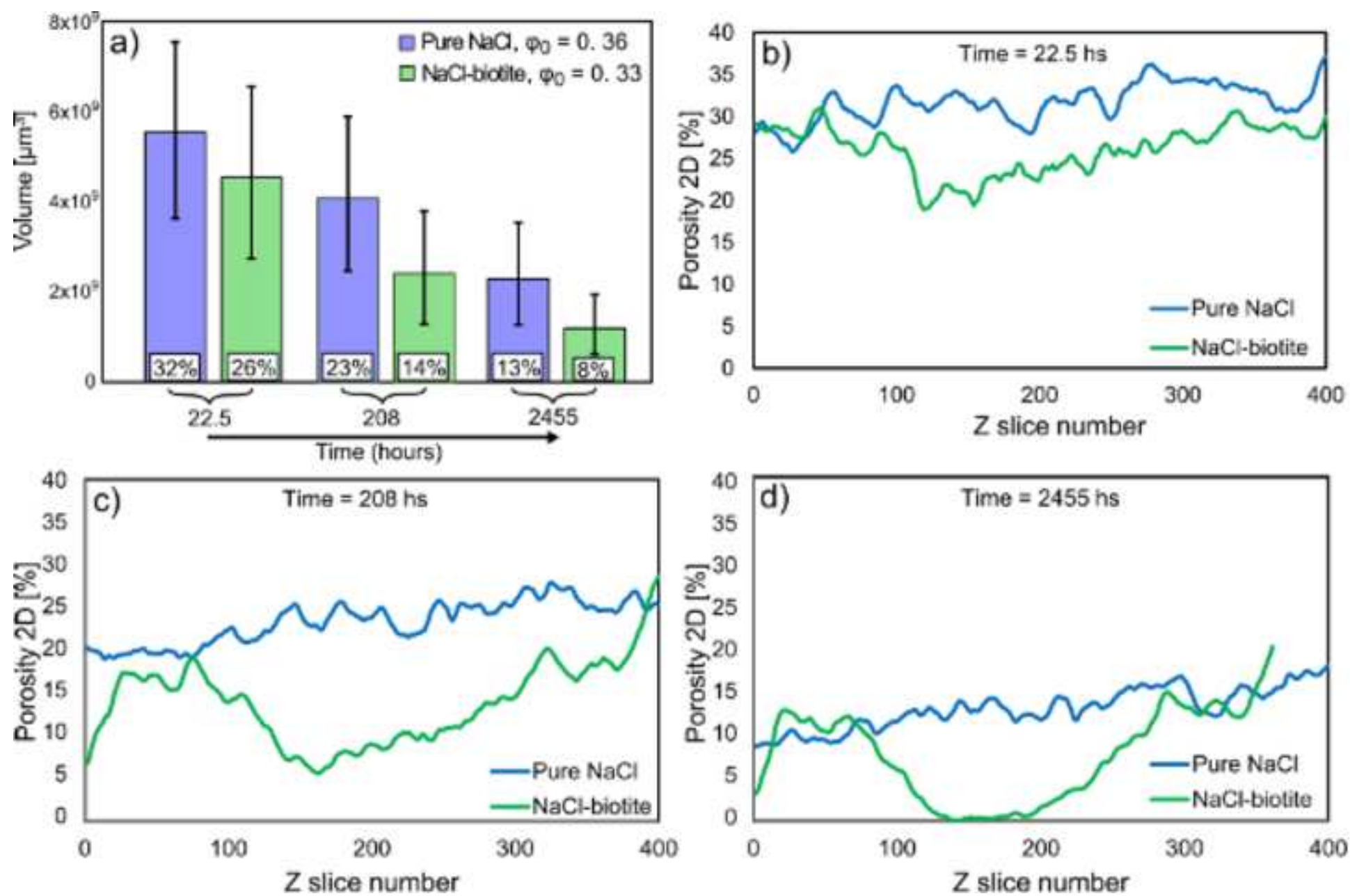


Figure 4

[Click here to download high resolution image](#)



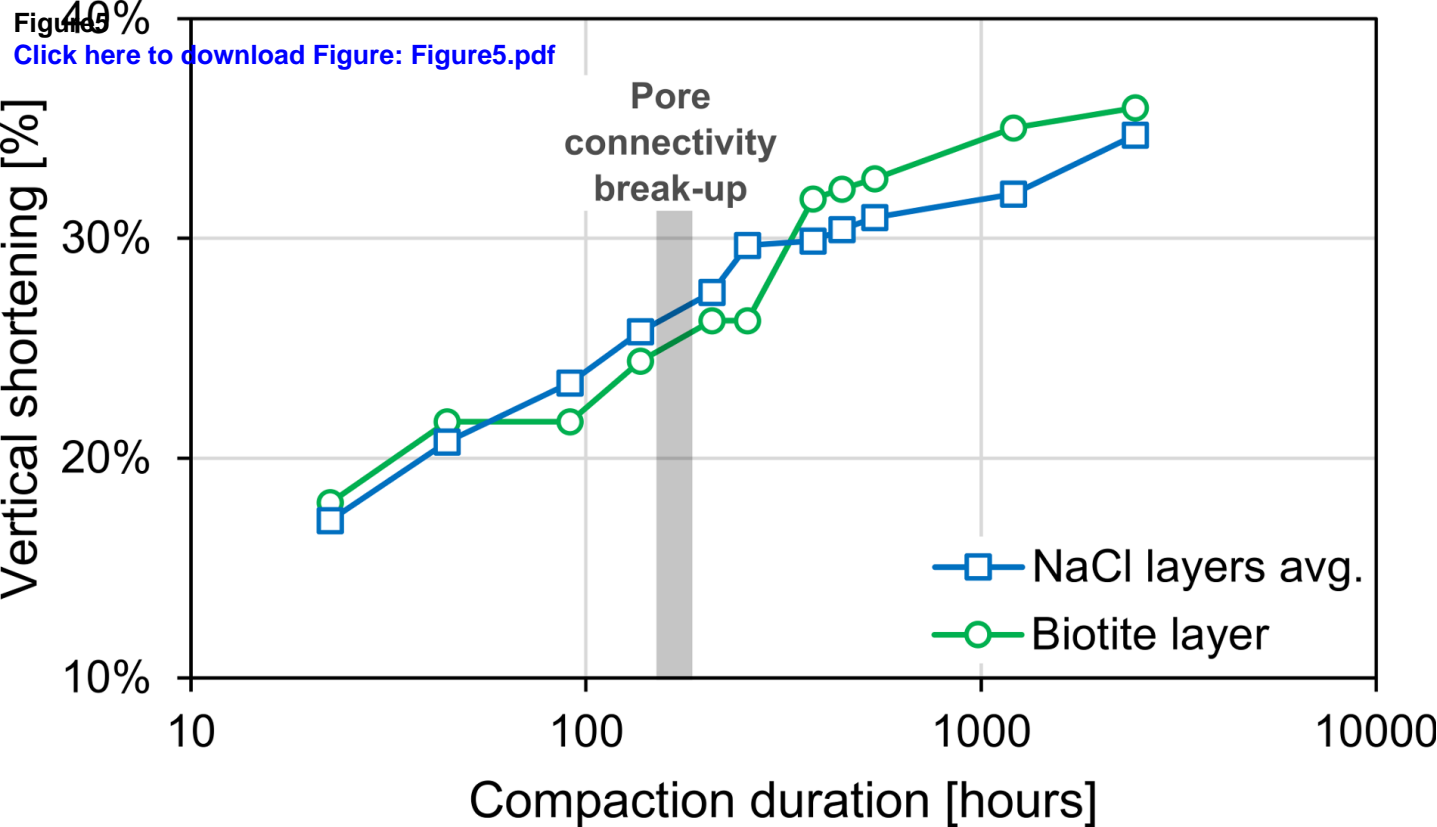




Figure6  
[Click here to download high resolution image](#)

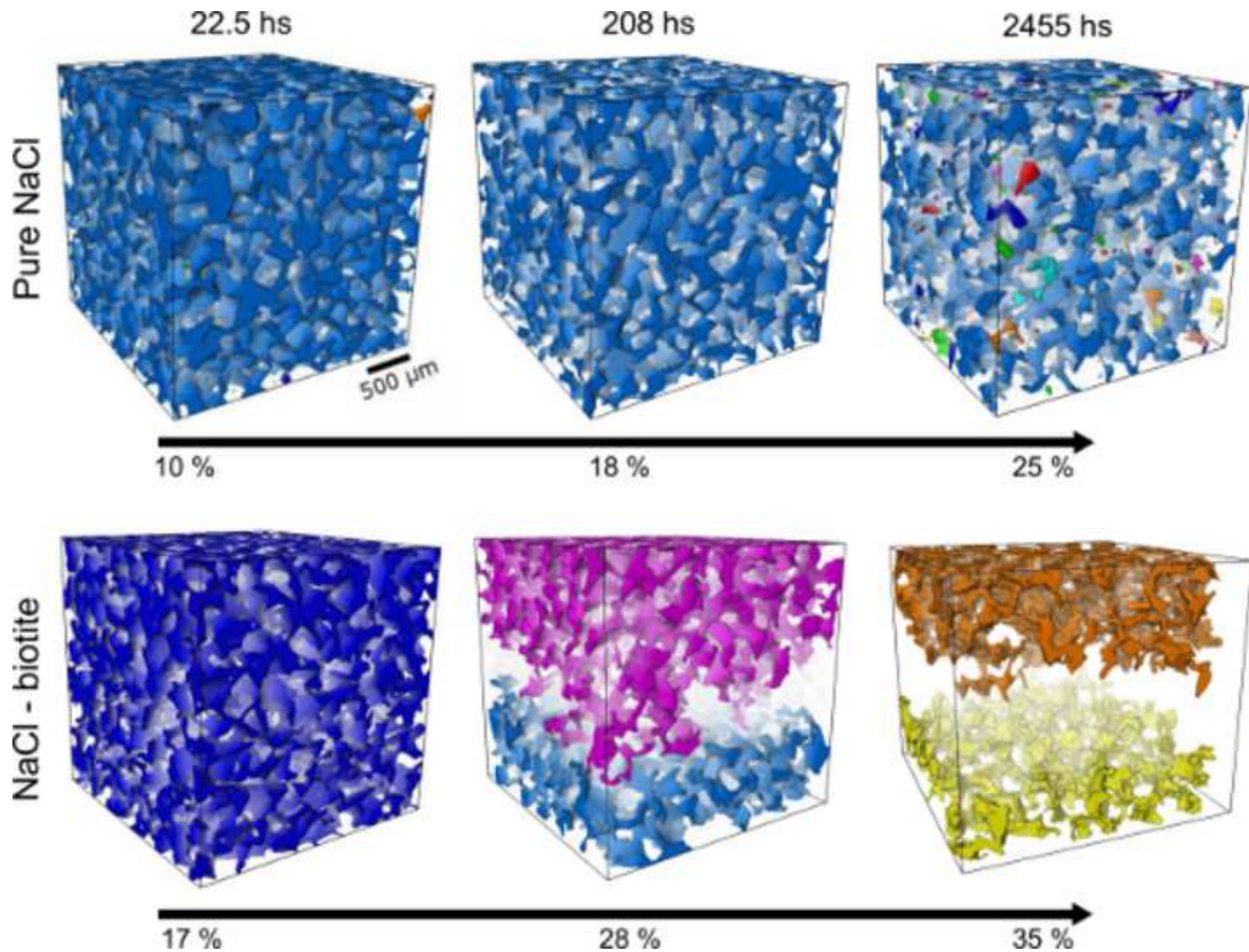


Figure7

[Click here to download high resolution image](#)

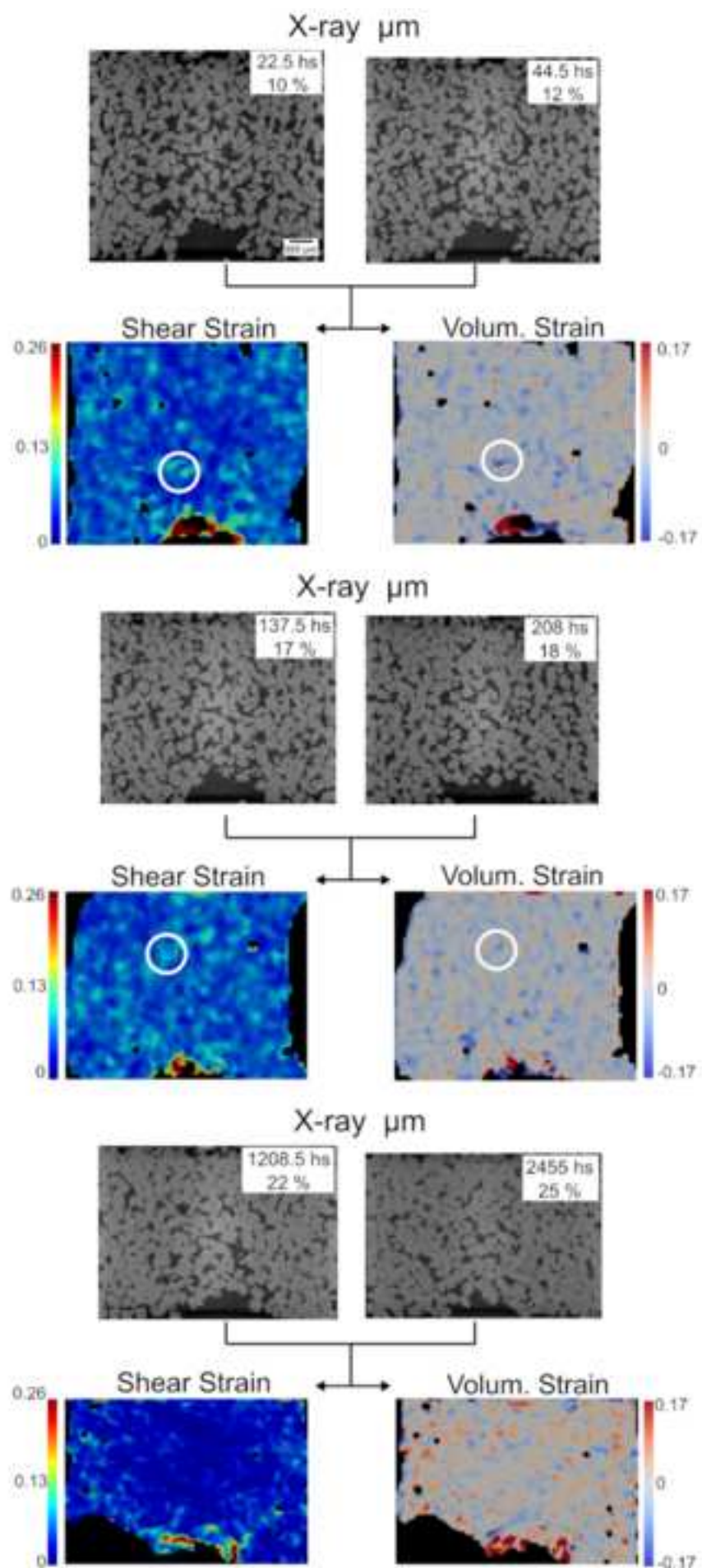




Figure8

[Click here to download high resolution image](#)

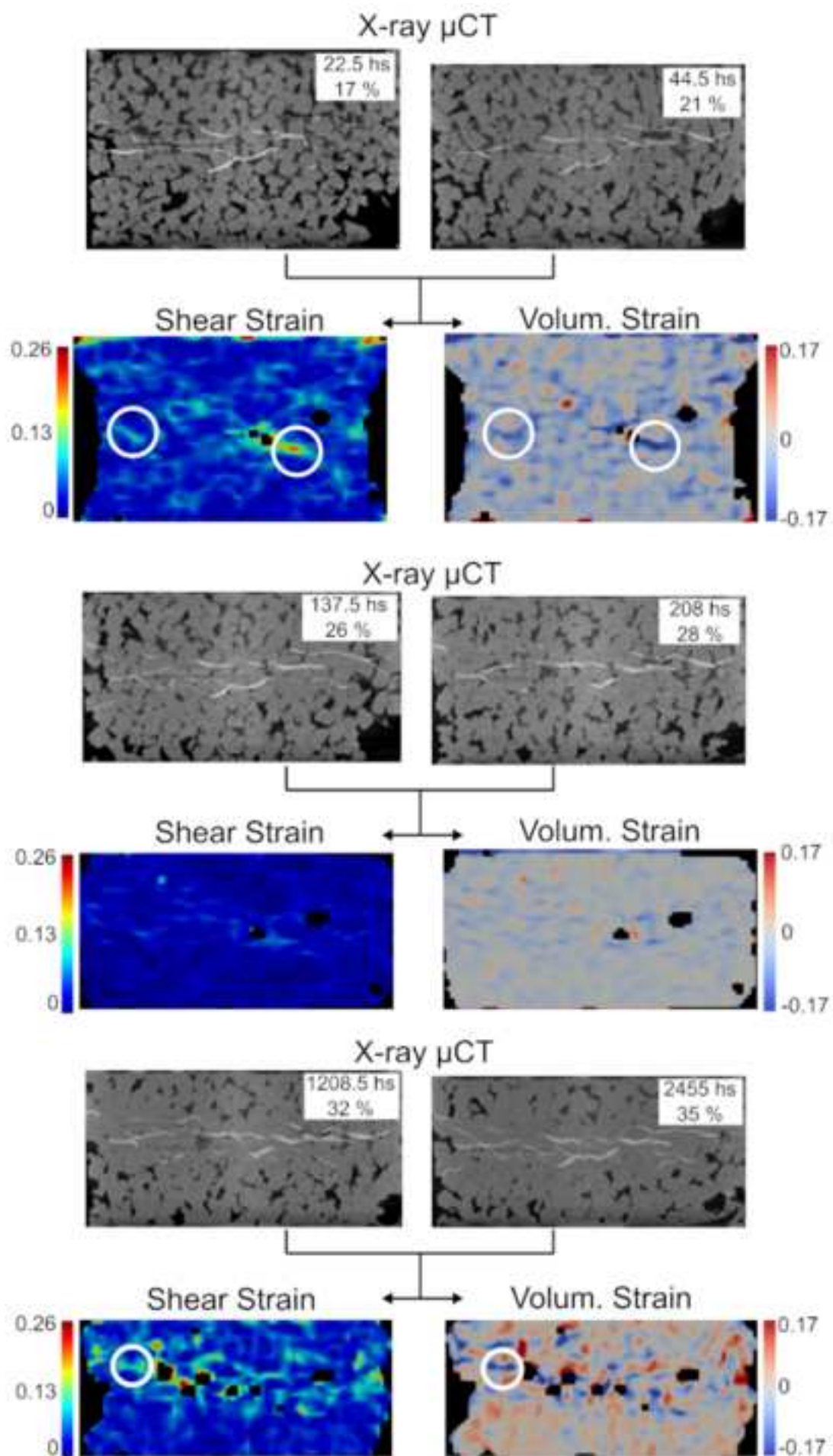


Figure9

[Click here to download high resolution image](#)

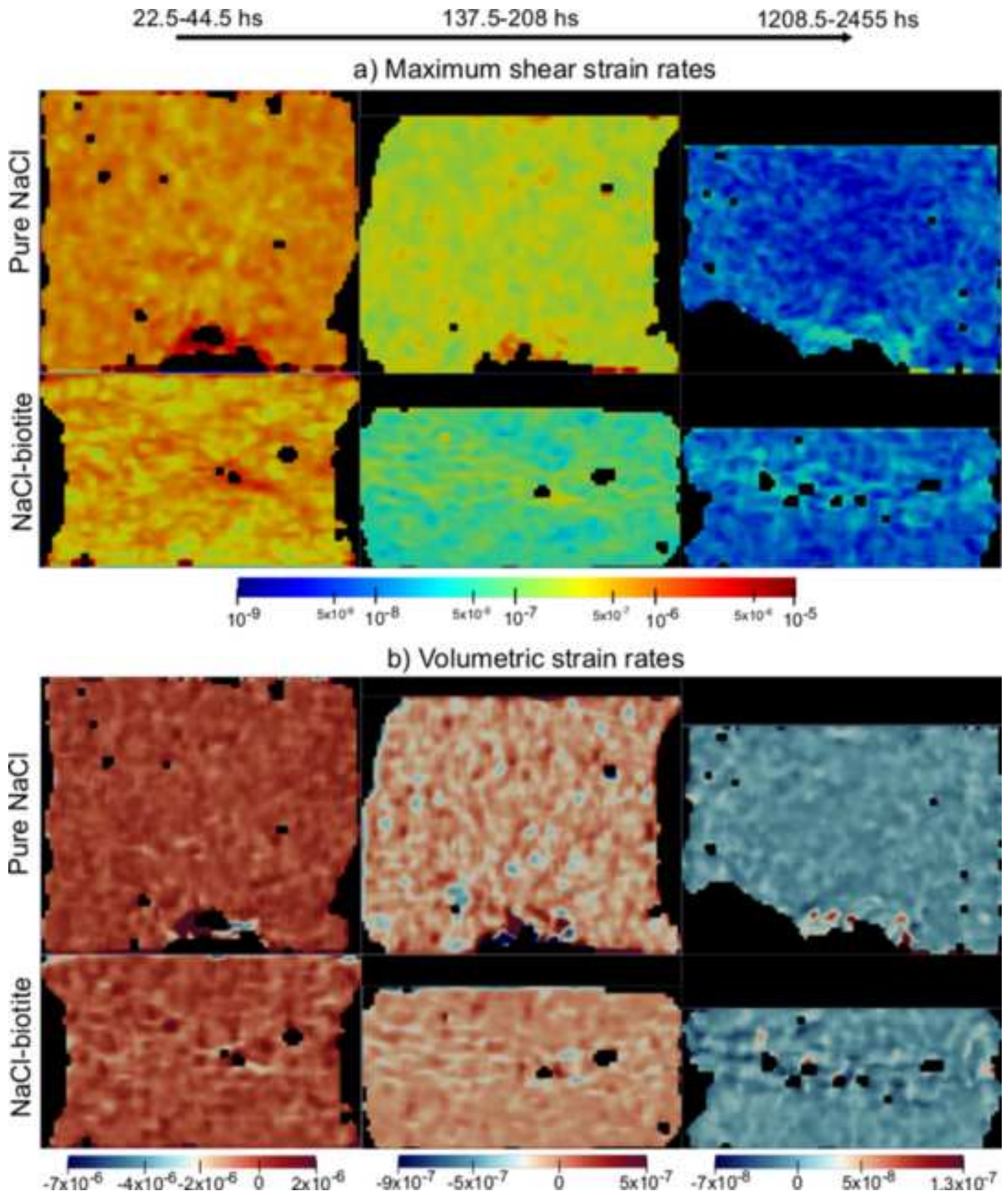
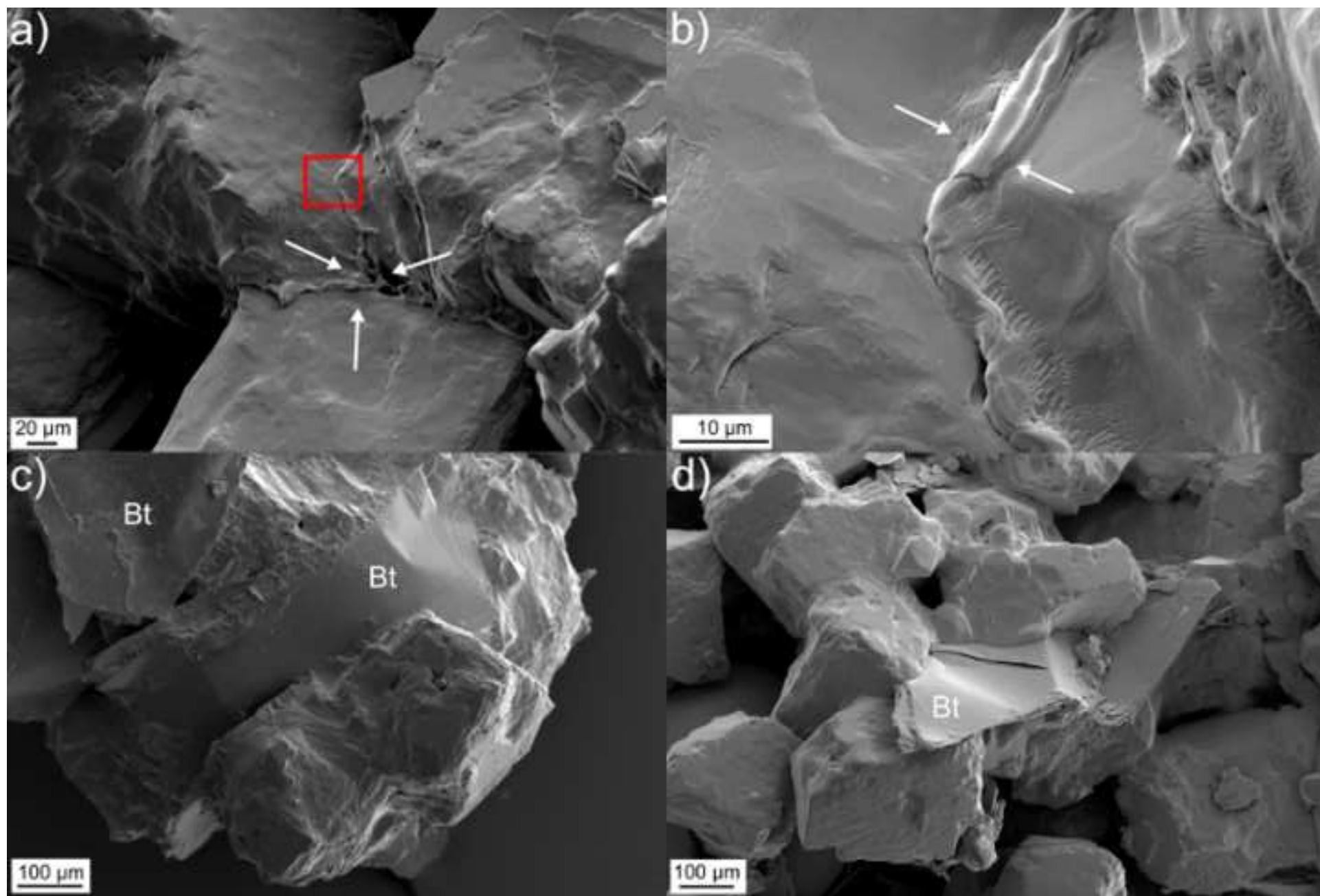




Figure10  
[Click here to download high resolution image](#)



**Figure 7(high-resolution)**

[Click here to download Figure \(high-resolution\): Figure7\(high-resolution\).tif](#)

**Figure 8(high-resolution)**

[Click here to download Figure \(high-resolution\): Figure8\(high-resolution\).tif](#)

**Figure 1(high-resolution)**

[Click here to download Figure \(high-resolution\): Figure1\(high-resolution\).tif](#)

**Figure 2(high-resolution)**

[Click here to download Figure \(high-resolution\): Figure2\(high-resolution\).pdf](#)

**Figure 3(high-resolution)**

[Click here to download Figure \(high-resolution\): Figure3\(high-resolution\).tif](#)

**Figure 4(high-resolution)**

[Click here to download Figure \(high-resolution\): Figure4\(high-resolution\).tif](#)

**Figure 5(high-resolution)**

[Click here to download Figure \(high-resolution\): Figure5\(high-resolution\).pdf](#)



**Figure 6(high-resolution)**

[Click here to download Figure \(high-resolution\): Figure6\(high-resolution\).tif](#)

**Figure 9(high-resolution)**

[Click here to download Figure \(high-resolution\): Figure9\(high-resolution\).tif](#)

**Figure 10(high-resolution)**

[Click here to download Figure \(high-resolution\): Figure10\(high-resolution\).tif](#)

**Supplementary material for online publication only**

**[Click here to download Supplementary material for online publication only: Macente2018\\_EPSL\\_SI\\_revised.docx](#)**

**Supplementary material GIF**

[Click here to download Supplementary material \(video\): Gif1.gif](#)

**Supplementary material GIF**

[Click here to download Supplementary material \(video\): Gif2.gif](#)